Dalton
Transactions

PAPER

View Article Online
View Journal | View Issue

Cite this: *Dalton Trans.*, 2015, **44**, 19232

Controlled ligand distortion and its consequences for structure, symmetry, conformation and spin-state preferences of iron(II) complexes†‡

Nicole Kroll,[a] Kolja Theilacker,[b] Marc Schoknecht,[a] Dirk Baabe,[c] Dennis Wiedemann,[a] Martin Kaupp,*[b] Andreas Grohmann*[a] and Gerald Hörner*[a]

The ligand-field strength in metal complexes of polydentate ligands depends critically on how the ligand backbone places the donor atoms in three-dimensional space. Distortions from regular coordination geometries are often observed. In this work, we study the isolated effect of ligand-sphere distortion by means of two structurally related pentadentate ligands of identical donor set, in the solid state (X-ray diffraction, ^{57}Fe-Mössbauer spectroscopy), in solution (NMR spectroscopy, UV/Vis spectroscopy, conductometry), and with quantum-chemical methods. Crystal structures of hexacoordinate iron(II) and nickel(II) complexes derived from the cyclic ligand L^1 (6-methyl-6-(pyridin-2-yl)-1,4-bis(pyridin-2-ylmethyl)-1,4-diazepane) and its open-chain congener L^2 (N^1,N^3,2-trimethyl-2-(pyridine-2-yl)-N^1,N^3-bis(pyridine-2-ylmethyl) propane-1,3-diamine) reveal distinctly different donor set distortions reflecting the differences in ligand topology. Distortion from regular octahedral geometry is minor for complexes of ligand L^2, but becomes significant in the complexes of the cyclic ligand L^1, where *trans* elongation of Fe–N bonds cannot be compensated by the rigid ligand backbone. This provokes trigonal twisting of the ligand field. This distortion causes the metal ion in complexes of L^1 to experience a significantly weaker ligand field than in the complexes of L^2, which are more regular. The reduced ligand-field strength in complexes of L^1 translates into a marked preference for the electronic high-spin state, the emergence of conformational isomers, and massively enhanced lability with respect to ligand exchange and oxidation of the central ion. Accordingly, oxoiron(IV) species derived from L^1 and L^2 differ in their spectroscopic properties and their chemical reactivity.

Received 1st July 2015,
Accepted 7th October 2015

DOI: 10.1039/c5dt02502h

www.rsc.org/dalton

Introduction

In vitro modelling of the biological function of a metal ion requires both an understanding of the factors governing its reactivity, and their control. An important determinant, which is often difficult to study in isolation from other factors, is the distortion of the ligand sphere as imposed by the biological matrix (*cf.* the concept of the entatic state[1,2]). Studies of entasis, both *in vivo* and *in vitro*,[3–7] are most numerous for copper-based redox catalytic systems. Here, catalytic activity is associated with the mismatch between actual coordination geometry and coordination chemical preference, which is tetrahedral for copper(I) and square planar (pyramidal) for copper(II). We posit that redox processes involving metal centres other than copper are similarly controlled by ligand-field distortion and therefore synthetically addressable. In particular, the electronic nature and reactivity of oxoiron(IV) species deriving from catalytically active iron(II) complexes, both *in vivo* and *in vitro*,[8–17] are expected to be highly susceptible to ligand-field effects. For instance, variation of the ligand-field strength has been used by Que *et al.* to tune the spin-state energetics of oxoiron(IV) in a functional model of taurine dioxygenase (TauD) through variation of a donor atom (N *vs.* O).[18]

In this work, we describe ligand-imposed distortion of the coordination environment as a powerful tool to tune the geometry, electronics and reactivity of a pair of iron(II) complexes. In two closely related N_5 ligands of identical donor atom set, distortion of the latter allows us to study the effects of changes

---

[a] *Technische Universität Berlin, Institut für Chemie, Sekr. C2, Straße des 17. Juni 135, 10623 Berlin, Germany. E-mail: Gerald.Hoerner@tu-berlin.de, Andreas.Grohmann@tu-berlin.de; Fax: +49 30 314 79656; Tel: +49 30 314 27936*
[b] *Technische Universität Berlin, Institut für Chemie, Theoretische Chemie/Quantenchemie, Sekr. C7, Straße des 17. Juni 135, 10623 Berlin, Germany. E-mail: Martin.Kaupp@tu-berlin.de; Fax: +49 30 314 21075; Tel: +49 30 314 79682*
[c] *Technische Universität Braunschweig, Institut für Anorganische und Analytische Chemie, Hagenring 30, 38106 Braunschweig, Germany. Fax: +49 531 391 5387; Tel: +49 531 391 5383*

† Dedicated to Professor Manfred Scheer on the occasion of his 60th birthday.

‡ Electronic supplementary information (ESI) available: Crystallographic data; selected structural details (XRD/DFT); additional figures. CCDC 1008832–1008837. For ESI and crystallographic data in CIF or other electronic format see DOI: 10.1039/c5dt02502h

in ligand-sphere geometry and symmetry. This approach decouples the metal centre under study from first-order ligand-field strength effects, as induced by donor set variation, either in terms of donor element (*e.g.*, N *vs.* O, *vide supra*) or in terms of hybridisation state within one class of donor atom (*e.g.*, sp^2 N *vs.* sp^3 N). Control of ligand-field strength[19] *via* incremental distortion of the geometry necessitates control of intra-ligand strain[20] and thus, synthesis of "tailor-made" polydentate ligands. In previous work, we have provided synthetic access to numerous polydentate nitrogen-dominated ligand systems[21,22] and have reported on structures and reactivity of their transition-metal complexes (*e.g.*, iron(II/III/V),[23–25] cobalt(II/III),[26] copper(II)[27]).

For the study presented here, we have prepared the cyclic ligand L^1 (6-methyl-6-(pyridin-2-yl)-1,4-bis(pyridin-2-ylmethyl)-1,4-diazepane),[28,29] and its open-chain congener L^2 (N^1,N^3,2-trimethyl-2-(pyridine-2-yl)-N^1,N^3-bis(pyridine-2-ylmethyl) propane-1,3-diamine). They both share the trisimine-bisamine donor set of the established pentadentate N_5 ligand *N*-benzyl-*N*,*N*′,*N*′-tris(pyridin-2-ylmethyl)-ethane-1,2-diamine (Bn-TPEN),[30,31] but differ in the connectivity and hence, structural flexibility of the central diamine unit (Scheme 1).

As is detailed here, structures and electronic properties of iron(II) complexes [FeL^n(X)] of these ligands reflect the differences in ligand topology and the inherent ligand-field strength of the co-ligand X. We have characterised the constitution, structure, and electronics of their iron(II) complexes in the solid state as well as in solution and by density-functional theory methods. Trigonal distortion of the coordination sphere, as a consequence of the angular constraint in L^1, is clearly shown to reduce the ligand-field strength significantly, thereby favouring electronic high-spin states of the iron(II) centres. Preliminary results indicate that ligand-imposed distortion also causes the related oxoiron(IV) species to show distinctly different spectroscopic properties and reactivity.

Results and discussion

Ligand synthesis

Synthetic details for the 1,4-diazepane-based ligand L^1 have been given in a previous publication.[29] The open-chain ligand L^2 was prepared from 2-methyl-2-(pyridine-2-yl)-propane-1,3-diamine[32] in four steps with an overall yield of *ca.* 40%, (Scheme 2). Experimental details and analytical results are given in the Experimental section.

^{1}H-NMR spectra of the ligands in $CDCl_3$ are unexceptional. A 2 : 1 intensity pattern in the pyridine-based resonances indicates (time-averaged) C_s symmetry in solution in both cases. The spectra of both ligands are overall similar. This suggests

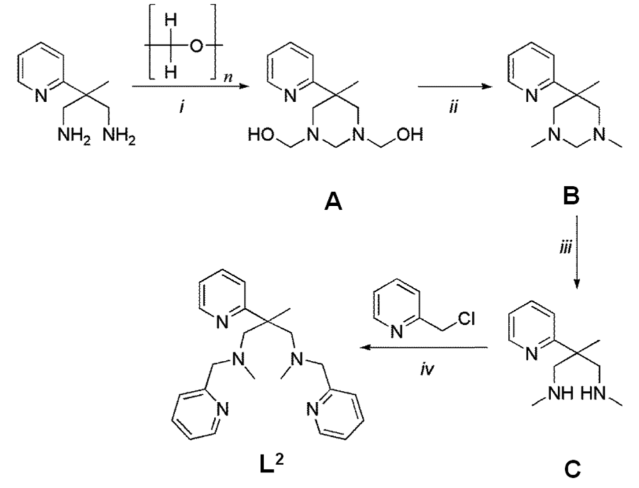

Scheme 2 Synthesis of the open-chain ligand L^2. (i) MeOH, RT, 1 d; (ii) $NaBH_4$, MeOH, RT (water bath), 1 d, AcOH; (iii) (a) HCl (32%), ethane-1,2-diol, 55 °C, 8 d, 180 mbar; (b) TFA, ethane-1,2-diol, 55 °C, 4 d, 180 mbar; (iv) Na_2CO_3, MeCN, 55 °C, 3 d.

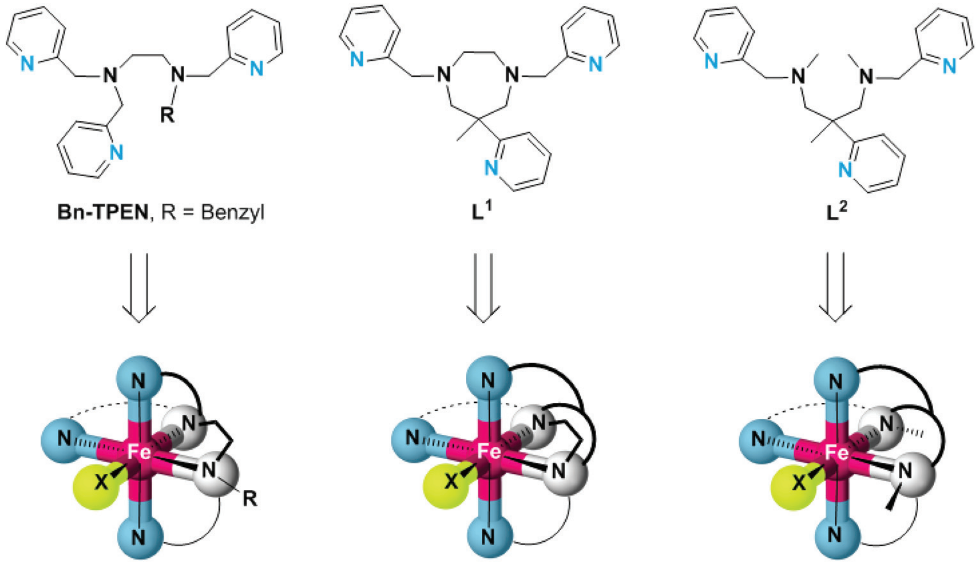

Scheme 1 Structures of the pentadentate N_5 ligands Bn-TPEN, L^1 and L^2, and structural sketches of the resulting hexacoordinate iron(II) complexes.

similar structural preferences in solution, *i.e.*, the structural constraints of the diazepane ring in L^1 (Scheme 1) do not restrict the conformational space of the picolyl donor groups to a significant extent.

Coordination chemistry of L^1 and L^2

Synthesis of metal complexes. Synthesis and structures of iron(II) complexes of ligand L^1 (≡ [**1**(X)]Y; with X = Cl, Br; Y = PF_6) have been described in a previous publication.[29] In the present work, we add two iron(II) complexes of ligand L^1, with X = Y = OTf and X = CH_3CN, Y = $(BPh_4)_2$, respectively. Complexation with $Fe(OTf)_2$ was performed in acetonitrile at room temperature. Single crystals of [**1**(OTf)](OTf) were grown by isothermal diffusion of diethyl ether into a solution of the resulting polycrystalline material (yellow powder) in dichloromethane. The acetonitrile complex $[\mathbf{1}(MeCN)]^{2+}$ was synthesised from the perchlorato precursor [**1**(ClO_4)](ClO_4) *via* ligand and anion metathesis. Dissolution of [**1**(ClO_4)](ClO_4) in methanol and treatment with excess $NaBPh_4$ afforded a yellowish powder. Single crystals of [**1**(MeCN)]$(BPh_4)_2$ were obtained by isothermal diffusion of diethyl ether into a solution of this powder in acetonitrile. Iron(II) complexes of ligand L^2 (≡ [**2**(X)]Y; with X = Cl, OTf; Y = PF_6, OTf) have been obtained by complexation of the open-chain ligand L^2 with $Fe(OTf)_2$ or $FeCl_2$. Generation of single crystals was performed as described for ligand L^1.

Crystal structures. All compounds crystallise as racemic mixtures of two helically chiral enantiomeric complex units. Crystallographic data can be found in Table S1.‡ The molecular structures of the complex ions $[\mathbf{1}(X)]^{n+}$ and $[\mathbf{2}(X)]^{n+}$ are summarised in Fig. 1. Representative structural data of the complex ions are given in Table 1. X-ray structure analysis reveals the expected function of L^1 and L^2 as pentadentate ligands, with the sixth coordination site occupied either by a coordinated anion or a solvent molecule. For the sake of structural comparison, the nickel(II) complexes $[NiL^1(ClO_4)](ClO_4)$ and $[NiL^2(OH_2)](ClO_4)_2$ have been synthesised and their solid-state structures analysed by X-ray crystallography (Fig. 1; characteristic bond lengths and angles are given in Table S2‡).

The coordination polyhedron of the iron(II) complexes is a (slightly distorted) octahedron in the case of $[\mathbf{2}(X)]^{n+}$, but fails to obey any regular geometry in the case of $[\mathbf{1}(X)]^{n+}$. The much stronger distortion of the coordination sphere in $[\mathbf{1}(X)]^{n+}$ is obviously due to constraints imposed by its cyclic ligand backbone. In particular, it is the 1,4-diazepane ring that forces and fixes the *cis* angle subtended by the amine-donor atoms at a value much smaller than the ideal value of 90°. As a consequence, the *cis*-angle distortion *Σ* (summed deviation of the 12

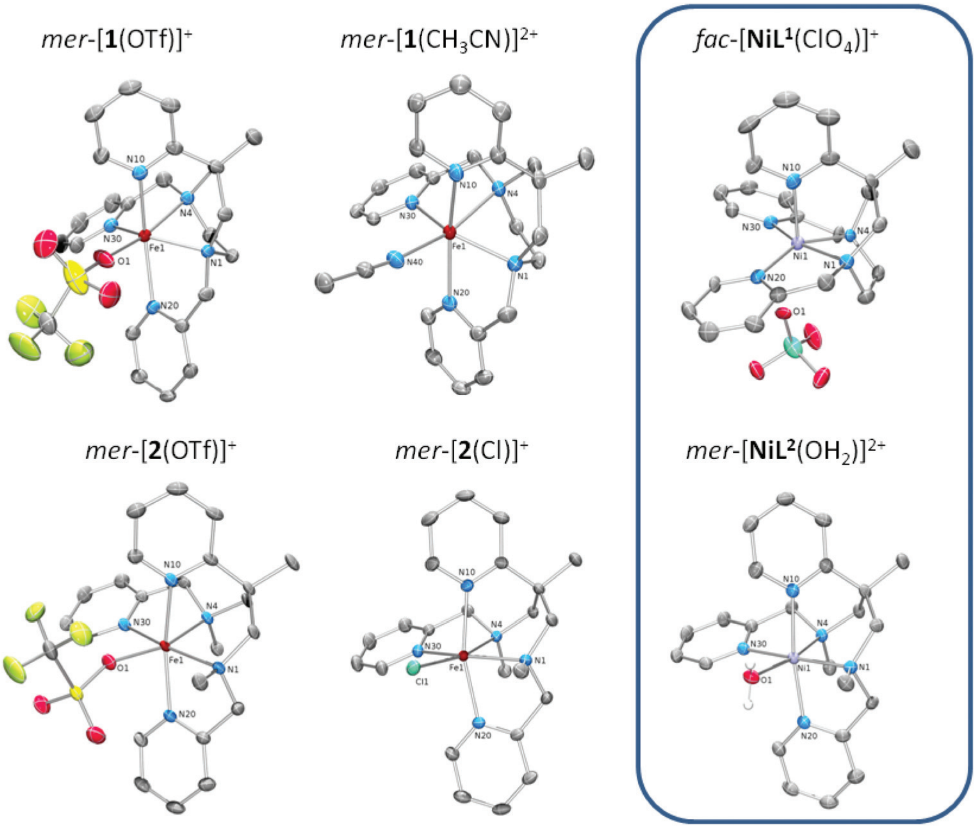

Fig. 1 Structures of the complex cations of iron(II) and nickel(II) complexes of the ligands L^1 (top) and L^2 (bottom)); '*mer*' and '*fac*' refer to the juxtaposition of the three pyridine donors (see Scheme 3). ORTEP representations with displacement ellipsoids at the 50% probability level; hydrogen atoms and counter ions omitted for clarity.

Table 1 Selected bond lengths (pm) and angles (°) for complexes [**1**(X)]Y and [**2**(X)]Y, and calculated distortion parameters Σ (°),[33] $S(O_h)$ and $S(TP)$[36]

	[**1**(X)]Y				[**2**(X)]Y	
	$X = Cl^-, Y = PF_6^{-\,a}$	$X = Br^-, Y = PF_6^{-\,a}$	$X = Y = OTf^-$	$X = MeCN, Y = (BPh_4^-)_2$	$X = Cl^-, Y = PF_6^-$	$X = Y = OTf^-$
Bond lengths						
Fe1–N1	218.78(17)	218.7(3)	218.0(2)	216.05(15)	223.12(16)	219.54(15)
Fe1–N4	233.73(17)	231.1(3)	227.4(2)	228.05(15)	233.01(15)	221.01(16)
Fe1–N10	216.25(18)	215.9(3)	215.8(2)	214.47(15)	218.37(15)	216.26(16)
Fe1–N20	226.33(18)	225.9(3)	226.3(2)	228.84(16)	216.92(15)	217.25(16)
Fe1–N30	213.17(18)	213.4(3)	213.2(2)	210.50(15)	220.00(16)	216.69(16)
Fe1–X	237.38(6)	253.97(6)	214.1(7)[b]	214.45(16)	238.84(5)	211.94(14)
Bond angles						
N1–Fe1–N4	71.15(6)	71.70(11)	72.50(8)	72.41(6)	86.56(6)	92.16(6)
N1–Fe1–N30	139.23(7)	140.16(12)	141.30(9)	141.08(6)	160.92(6)	169.10(6)
N4–Fe1–X	167.17(5)	168.04(8)	167.7(4)	166.61(6)	166.66 (4)	163.31(6)
N10–Fe1–N20	165.00(7)	164.63(11)	158.92(9)	163.91(6)	163.27 (6)	163.21(6)
Distortion parameters						
$\Sigma/°$	134.0	142.1	145.0[b]	140.4	89.8	81.1
Δd_{eq}/pm[c]	13.1	12.5	13.1	18.3	6.2	3.2
N_4 torsion[d]			50.2	44.8	11.1	13.9
$S(O_h)$[e]	5.09	5.22	5.95[b]	4.80	1.86	1.84
$S(TP)$[f]	7.38	7.96	5.19	6.45	11.31	10.06

[a] Data from ref. 29. [b] Oxygen atom O1 is disordered over two positions (O1A, O1B): parameters involving O1A are given in the table; d(Fe1–O1B) = 204.5(8) pm; angle(N1–Fe1–O1B) = 167.3(3)°; Σ = 149.3° (for O1B); $S(O_h)$ = 5.15 (for O1B). [c] Fe–N bond-length variation in the N_4 equatorial plane. [d] N10/N20/N30/N1 torsion angle. [e] Continuous shape measure for octahedral coordination. [f] Continuous shape measure for trigonal prismatic coordination.

cis angles in the polyhedron from 90°)[33] is substantially higher for $[\mathbf{1}(X)]^{n+}$ than in $[\mathbf{2}(X)]^{n+}$.

Iron–nitrogen bond lengths are in the range 210 pm < d(Fe–N) < 235 pm in all cases (see Table 1). This clearly indicates iron(II) in its high-spin electronic configuration (hs, $S = 2$, $t_{2g}^4e_g^2$),[34,35] irrespective of both the nature of the N_5 ligand and the identity of the co-ligand. It is noted, however, that UV/Vis and ^{1}H-NMR data of $[\mathbf{2}(MeCN)]^+$ in acetonitrile solution at low temperature and Mössbauer spectra of powder samples of $[\mathbf{2}(MeCN)](OTf)_2$ reveal significant contributions of low-spin iron(II) (ls, $S = 0$, $t_{2g}^6e_g^0$) (*vide infra*). While XRD data of the acetonitrile complex of L^2 are as yet unavailable (single crystals could not be obtained), its behaviour in solution and in the solid state resembles the closely related N_5 ligand Bn-TPEN, whose iron(II) complex with coordinated acetonitrile $[Fe(Bn\text{-}TPEN)(CH_3CN)]^{2+}$ shows low-spin characteristics in the solid state and in solution.[30]

The Fe–N bonds *trans* to the co-ligands X, which involve one of the amine N atoms, are elongated in the solid-state structures (Fe1–N4 in Fig. 1 and Table 1) owing to the operation of a strong *trans* influence. This causes secondary structural effects, which are distinctly different between the two types of N_5 ligand.

Firstly, complexes of the ring-derived ligand L^1 show substantial scatter among the Fe–N bond lengths in the N_4 equatorial plane. In Fig. 2a, for both $[\mathbf{1}(X)]^{n+}$ and $[\mathbf{2}(X)]^{n+}$, the maximum variation in the bond lengths, Δd_{eq}, is illustrated by a plot against the (essentially invariant) average Fe–N bond lengths in the N_4 equatorial plane, $\bar{d}_{eq}$. Secondly, there is massive distortion from planarity within this N_4 donor set only in the case of $[\mathbf{1}(MeCN)](OTf)_2$ (torsion amounts to 50°; Fig. S1‡). In conclusion, angular distortion and bond-length scatter are correlated with each other. Both reflect the different degrees of structural feedback within the ligands.

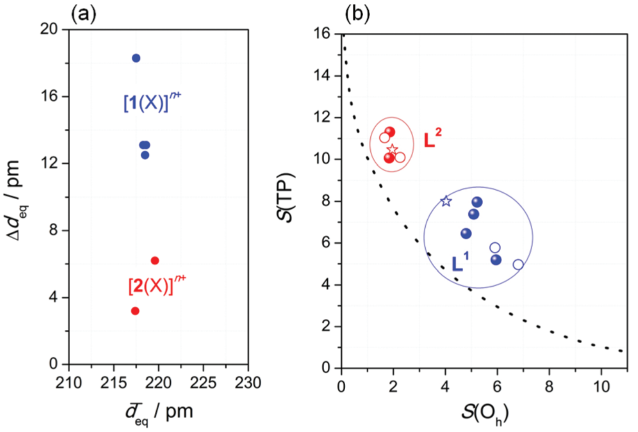

Fig. 2 Ligand-imposed distortion of the coordination sphere: (a) Bond-length variation Δd_{eq} within the N_4 equatorial plane; (b) continuous shape map of the octahedron ↔ trigonal prism transition (see text); blue: $[\mathbf{1}(X)]^{n+}$; red: $[\mathbf{2}(X)]^{n+}$; line: ideal Bailar twist; filled: XRD-derived structures; open: DFT-optimised structures (B3LYP-D3/def2-TZVP/COSMO(MeCN)); stars: crystal structures of the Ni(II) complexes from Fig. 1.

This having been said, the distorted structure of $[\mathbf{1}(X)]^{n+}$ can be analysed as a blend of octahedral and trigonal-prismatic arrangements; *i.e.*, the trigonal Bailar twist angle θ between co-facial donor triads (see Fig. S2‡) amounts to 27.5°, intermediate between an ideal octahedron (θ = 60°) and a regular trigonal prism ($\theta = 0°$). Thus, the spatial arrangement of donor atoms in L^1 supplies the central atom with a ligand field poised between tetragonal and trigonal symmetry. This conclusion is supported by an analysis of continuous symmetry/shape measures $S(O_h)$ and $S(\mathrm{TP})$,[36,37] which quantify the deviation from regular octahedral and trigonal-prismatic geometry, respectively.

In Fig. 2b, the $S(O_h)$ and $S(\mathrm{TP})$ values of the iron(II) complexes (from Table 1; DFT-derived data from Table S3‡) are given as a continuous shape map of the octahedron ↔ trigonal prism transition along the trigonal Bailar twist (line).[38] Evidently, the complexes of either ligand are in distinctly separated regions of this map. The values for $S(O_h)$, which is zero for an ideal octahedron, cluster around $S(O_h) = 6 \pm 1$, for complexes $[\mathbf{1}(\mathrm{X})]^{n+}$ of the constrained ligand L^1, but are substantially smaller for complexes $[\mathbf{2}(\mathrm{X})]^{n+}$ of the open-chain ligand L^2 ($S(O_h) = 2.0 \pm 0.5$).

Characterisation of $[\mathbf{1}(\mathrm{X})]^{n+}$ and $[\mathbf{2}(\mathrm{X})]^{n+}$ in solution

Solutions of $[\mathbf{1}(\mathrm{X})]^{n+}$ and $[\mathbf{2}(\mathrm{X})]^{n+}$ in acetonitrile and dichloromethane have been characterised by ^{1}H- and ^{19}F-NMR spectroscopy, AC conductometry, and UV/Vis spectroscopy. The results are summarised in Table 2.

Speciation. The chemical reactivity of hexacoordinated complexes with pentadentate ligands necessarily reflects the lability of the co-ligand X with respect to substitution.[22] The speciation of the complexes under study was therefore expected to be solvent-dependent. Speciation of the iron(II) complexes $[\mathbf{1}(\mathrm{OTf})]^+$ and $[\mathbf{2}(\mathrm{OTf})]^+$ has been studied by means of ^{19}F-NMR spectroscopy (Fig. S3‡; [Fe] ≈ 15 mmol L^{-1}) and conductometric measurements ([Fe] = 1.3 mmol L^{-1}) in acetonitrile and dichloromethane solutions. The weakly coordinating triflato ligands, both in $[\mathbf{1}(\mathrm{OTf})]^+$ and $[\mathbf{2}(\mathrm{OTf})]^+$, are actually found to be exchanged for solvent in neat acetonitrile, but remain coordinated in neat dichloromethane.

Both types of experiment indicate the dissociation of coordinated triflate upon solvation in acetonitrile. ^{19}F-NMR spectra of both compounds in (D$_3$)-acetonitrile show a single resonance located at $\delta = -72.9$ ppm and −79.0. ppm for $[\mathbf{1}(\mathrm{X})]^{n+}$ and $[\mathbf{2}(\mathrm{X})]^{n+}$, respectively. The peak width (fwhm; full-width at half-maximum) is *ca.* 15 Hz in both cases. Spectral signature, chemical shifts and peak width are as expected for free triflate ion.[39,40] A molar conductivity in the range 227 S mol^{-1} cm^2 < Λ < 277 S mol^{-1} cm^2 indicates the (predominant) presence of a 2 : 1 electrolyte, and thus the formation of di-cationic complexes upon dissolution of the triflato complexes in acetonitrile, most probably $[\mathbf{1}(\mathrm{CH_3CN})]^{2+}$ and $[\mathbf{2}(\mathrm{CH_3CN})]^{2+}$.

Table 2 Speciation and spectroscopic data for dissolved [**1**(OTf)](OTf) and [**2**(OTf)](OTf) at room temperature

	[**1**(OTf)](OTf)		[**2**(OTf)](OTf)	
Solvent Dominant Species	DCM $[\mathbf{1}(\mathrm{OTf})]^+$	MeCN $[\mathbf{1}(\mathrm{MeCN})]^{2+}$	DCM $[\mathbf{2}(\mathrm{OTf})]^+$	MeCN $[\mathbf{2}(\mathrm{MeCN})]^{2+}$
NMR				
δ_H [ppm]	[−2; 115]	[−5; 92]	[−7; 86]	[−1; 44] [1.5; 9.8]^a
δ_F [ppm]/fwhm [Hz]	−76.0/18 −1.8/38	−72.9/16	−76.2/18 −2.0/39	−79.0/13
Conductometry				
Λ [S mol^{-1} cm^2]^b	18.5	228	15.4	276
UV/Vis				
λ_max [nm]	372	370	—	398
ε_max [cm^{-1} L mol^{-1}]	1.200	1.100	—	6.700

^{a} Measured at T = 233 K. ^{b} Concentration $c = 1.3 \times 10^{-3}$ mol L^{-1}.

In (D$_2$)-dichloromethane solution, the ^{19}F-NMR spectra of $[\mathbf{1}(\mathrm{X})]^{n+}$ and $[\mathbf{2}(\mathrm{X})]^{n+}$ consist of two signals of equal area, indicating two different chemical environments for triflate in solution in both cases. A resonance at −76 ppm with a fwhm = 18 Hz is characteristic of free triflate, whereas a significantly broadened singlet, shifted strongly downfield at $\delta = -2$ ppm, is attributable to coordinated triflate. Fully consistent with predominating mono-cationic complexes, most probably $[\mathbf{1}(\mathrm{OTf})]^+$ and $[\mathbf{2}(\mathrm{OTf})]^+$, a molar conductivity in the range 15 S mol^{-1} cm^2 < Λ < 19 S mol^{-1} cm^2 suggests the presence of a 1 : 1 electrolyte.[41] The speciation of the complexes in solution is fully corroborated by ^{57}Fe-Mössbauer spectroscopic studies of powder samples prepared from these solutions *via* rapid precipitation (*vide infra*).

Spin state. The visual appearance of the complex salts [**1**(OTf)](OTf) and [**2**(OTf)](OTf) is very similar in the solid state. Whereas the faint yellow colour of [**1**(OTf)](OTf) is conserved in acetonitrile solution (λ_max = 370 nm; ε_max = 1100 cm^{-1} L mol^{-1}), [**2**(OTf)](OTf) shifts to an intensely red-orange colour upon contact with acetonitrile. UV/Vis spectra (UV/Vis data in Table 2; spectra in Fig. 3a) of the resulting dilute solutions of $[\mathbf{2}(\mathrm{MeCN})]^{2+}$ are dominated by an intense absorption at 400 nm (ε_max = 6700 cm^{-1} L mol^{-1}). This signature is strongly reminiscent of the solution spectra of the ls-

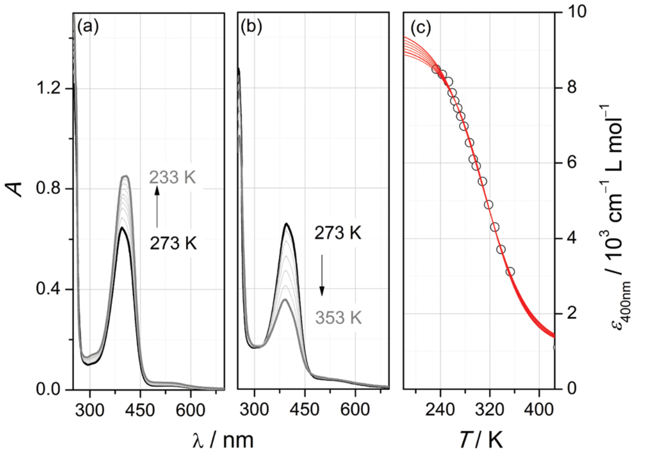

Fig. 3 Variable-temperature UV/Vis spectra of [**2**(MeCN)](OTf)$_2$ in acetonitrile ($c = 1.0 \times 10^{-3}$ mol L^{-1}; light path d = 0.1 cm) with (a) decreasing temperature, (b) rising temperature; (c) temperature dependence of the molar absorption coefficient at λ = 400 nm (lines: sigmoidal fits with 9000 < ε_ls [cm^{-1} L mol^{-1}] < 9600 and ε_hs = 1100 cm^{-1} L mol^{-1}).

Table 3 Electronic SCO energies ($\Delta_{SCO}E_{el} = E_{el}$ (ls) − E_{el} (hs), in kJ mol^{-1}) in $[\mathbf{1}(X)]^{n+}$ and $[\mathbf{2}(X)]^{n+}$ (from DFT calculations)

	L^1	L^2
X = OTf	+50.8 (+36.0)	+22.6 (+15.4)
X = MeCN	+23.6 (+4.0)	−2.4 (−23.9)

B3LYP-D3/def2-TZVP/COSMO(MeCN)//B3LYP-D3/def2-TZVP/COSMO-(MeCN). Values in parentheses: B3LYP*/def2-TZVP/COSMO(MeCN)// B3LYP-D3/def2-TZVP/COSMO(MeCN).

iron(II) complex [Fe(Bn-TPEN)(MeCN)]$^{2+}$ (λ_{max} = 390 nm; ε_{max} = 8892 cm^{-1} L mol^{-1}),[30] and is accordingly interpreted as being due to an MLCT transition within a ls-iron(II) species.

In agreement with this assignment, the intensity of the band is affected by temperature: at low temperature (Fig. 3a), a further increase to ε_{max} = 8400 cm^{-1} L mol^{-1} accompanies a slight red-shift to λ_{max} = 406 nm, whereas at elevated temperature (Fig. 3b), the band is successively bleached and blue-shifted (λ_{max} = 388 nm at T = 353 K). This behaviour is typical of thermal spin-crossover (SCO) systems (eqn (1)).

$$\text{ls-}[\mathbf{2}(\text{MeCN})]^{2+} \rightleftharpoons \text{hs-}[\mathbf{2}(\text{MeCN})]^{2+} \tag{1}$$

In order to extract the thermodynamic parameters of the SCO-induced thermochromism of [**2**(MeCN)]$^{2+}$, UV/Vis absorption at λ = 400 nm has been analysed at temperatures between 233 K and 353 K. Because of solvent-inherent limitation of the temperature range, the absorption coefficient of the ls-form was estimated through sigmoidal fitting of the data to a Boltzmann model (Fig. 3c; the array of curves denotes fits with ε(ls) fixed to values between 9000 and 9600 cm^{-1} L mol^{-1}). Van't Hoff analysis of the SCO equilibrium constants that derive from these data (Fig. S4‡) reflects the uncertainty in the absorption coefficients. Within the given range of ε(ls), the enthalpy and entropy of SCO vary between $\Delta_{SCO}H_m$ = 19.8–22.7 kJ mol^{-1} and $\Delta_{SCO}S_m$ = 64.8–72.8 J K^{-1} mol^{-1}, respectively, with a turnover temperature $T_{1/2}$ = 310(5) K.

Our interpretation of the thermochromism of [**2**(MeCN)]$^{2+}$ in terms of an SCO equilibrium between hs and ls forms is corroborated by the temperature dependence of its ^{1}H-NMR spectra in (D$_3$)-acetonitrile (Fig. S5‡). The proton resonances in the room-temperature spectrum are widely spread between 44 ppm > δ > −1 ppm and substantially broadened (typically 300 Hz > fwhm > 70 Hz) with respect to the spectrum of the free ligand. These findings indicate the presence in solution of paramagnetic species. On decreasing the temperature, the spectral range of resonances becomes successively narrower, accompanied by narrowing of the individual resonance profiles. At T = 233 K, close to the freezing point of (D$_3$)-acetonitrile, sharp lines with partially resolved J_{HH} coupling patterns are recorded within the range of 10 ppm > δ > 1 ppm; that is, the SCO equilibrium has shifted to the diamagnetic ls form of [**2**(MeCN)]$^{2+}$.

By contrast, both the ^{1}H-NMR and UV/Vis spectra (λ_{max} = 370 nm; ε_{max} = 1100 cm^{-1} L mol^{-1} at T = 233 K and 298 K) of [**1**(OTf)](OTf) solutions in acetonitrile clearly indicate the resulting acetonitrile complex to be a high-spin species. This is a consequence of conformational constraints in L^1 and is reproduced by computed electronic energies of the SCO (Table 3).

Optimisations with the B3LYP hybrid functional slightly favour the singlet over the quintet state for [**2**(MeCN)]$^{2+}$ but provide a clear preference for the quintet in case of [**1**(MeCN)]$^{2+}$ (Table 3). As B3LYP SCO energies had been found previously to artificially favour the hs forms,[42] we have also carried out single-point calculations with the modified B3LYP* functional with 15% rather than 20% Hartree-Fock exchange. This functional had been suggested previously to better describe SCO in Fe(II) complexes.[42] At B3LYP* level, the singlet preference for [**2**(MeCN)]$^{2+}$ is more pronounced, the quintet preference for [**1**(MeCN)]$^{2+}$ much smaller (Table 3). Yet, the computed overall difference in the SCO energies of the two complexes remains almost constant around 27 kJ mol^{-1}. The weaker ligand field of the co-ligand OTf in [**1**(OTf)]$^+$ and [**2**(OTf)]$^+$ translates into a clear energetic preference for the hs state in both complexes, while comparison of the absolute values signals a marked dependence on the input of the respective N$_5$ ligand.

With the array of electronic SCO energies in hand (Table 3), it was possible to isolate the incremental contributions ascribable to the N$_5$ ligand ($\delta\Delta_{SCO}E_{el}$(N$_5$)) and the co-ligand ($\delta\Delta_{SCO}E_{el}$(X)). Interestingly, both factors are found to contribute similarly to the SCO energies. The incremental contribution of the co-ligand $\delta\Delta_{SCO}E_{el}$(X) (vertical difference in Table 3) amounts to *ca.* 25–27 kJ mol^{-1}, whereas the distortion-related increment of the N$_5$ ligand $\delta\Delta_{SCO}E_{el}$(N$_5$) (horizontal difference in Table 3) amounts to *ca.* 26–28 kJ mol^{-1}. The latter value is a good measure of the difference in d-orbital splitting between the ligand fields as supplied by L^1 and L^2, in fair agreement with energy differences derived from UV/Vis spectroscopy (*vide infra*).

As single crystals of [**2**(MeCN)](OTf)$_2$ could not be obtained, the spin state of this compound in the solid state has been studied by ^{57}Fe-Mössbauer spectroscopy on polycrystalline (powder) samples. Powders of the triflato complex [**2**(OTf)]-(OTf) were taken as a reference system with temperature-invariant hs character. Mössbauer spectra of [**2**(OTf)](OTf) and [**2**(MeCN)](OTf)$_2$ were recorded at $T \approx$ 100 K (Fig. 4a and b) and analysed by least-squares fitting with doublets of Lorentzian lines. The results with focus on the main components of the Mössbauer spectrum are summarised in Table 4. The results corroborate our spin-state assignments from the solution studies and agree with the implications of the DFT-derived SCO energies.

The Mössbauer spectra of [**2**(OTf)](OTf) were analysed by use of three sub-spectra (Fig. 4b), whereby the main signal (volume fraction >80%) with an isomer shift of δ = 1.088 mm s^{-1} and quadrupole splitting of ΔE_Q = 2.123 mm s^{-1} is clearly attributable to a hs iron(II) complex, which corroborates the results of the solution studies of spin state and speciation discussed above. Minor amounts of ls iron(II) (volume fraction

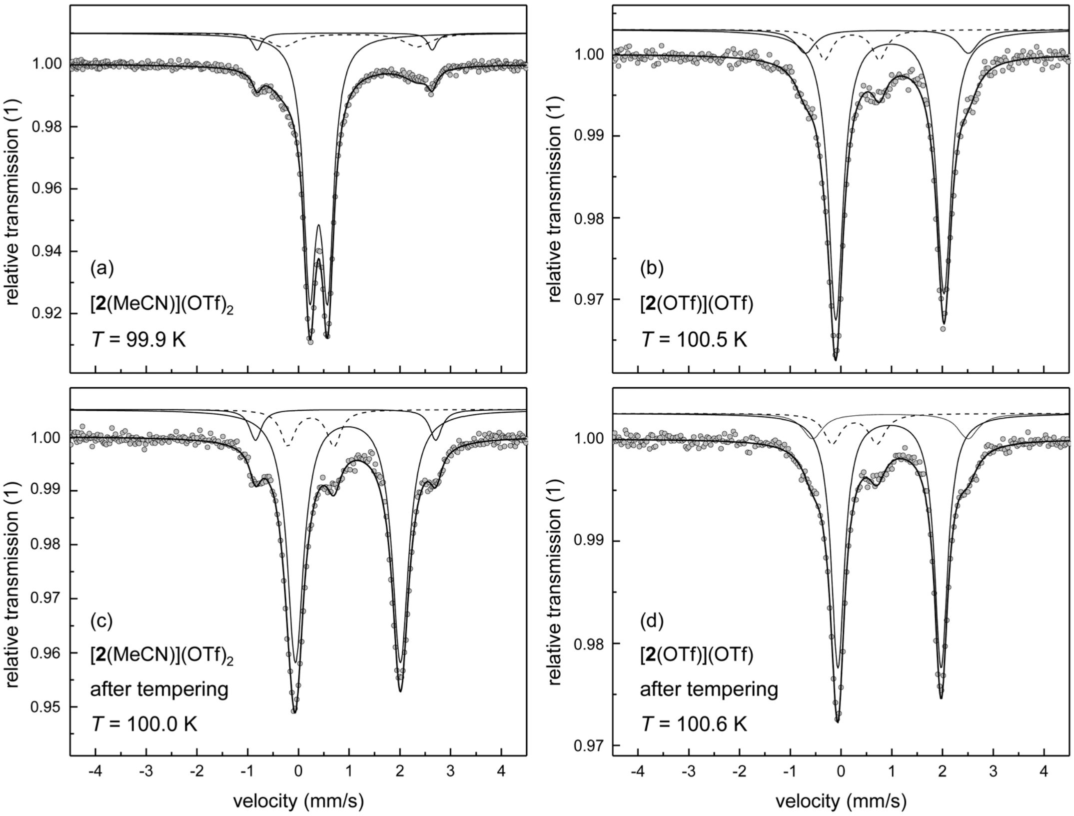

Fig. 4 Mössbauer spectra at $T \approx 100$ K of powder samples obtained by precipitation from solutions of [**2**(OTf)](OTf) (Symbols: experimental data; lines: fit; for clarity the sub-spectra are plotted with an offset against the *y* axis): (a) [**2**(MeCN)]$(OTf)_2$ from MeCN solution; (b) [**2**(OTf)](OTf) from dichloromethane solution; (c) sample from (a) after tempering at $T = 350$ K for three days under reduced pressure; (d) sample from (b) after tempering at $T = 350$ K for four days under reduced pressure.

≈9%) with isomer shift of $\delta = 0.342$ mm s^{-1} and quadrupole splitting of $\Delta E_Q = 1.077$ mm s^{-1} are assigned to a thermally trapped residual ls iron(II) form of [**2**(OTf)](OTf); a small amount of hs iron(II) (volume fraction ≈9%) is associated with an impurity, which has been introduced in the preparation process.

The material formulated as [**2**(MeCN)]$(OTf)_2$, as deduced from ^{19}F-NMR spectra, thermochromism and elemental analysis, gives Mössbauer spectra typical of ls iron(II) complexes with only minor distortions from octahedral geometry (Fig. 4a). The major component of the spectrum (volume fraction >80%) provides a doublet of small isomer shift of δ = 0.520 mm s^{-1} and quadrupole splitting of $\Delta E_Q = 0.353$ mm s^{-1}. The additional signals in the spectrum with larger splitting indicate minor amounts of two different residual hs iron(II) species. The signal with approx. 4% volume fraction (ΔE_Q = 3.452 mm s^{-1}) is associated with an impurity, as described for [**2**(OTf)](OTf). The second hs signal with *ca.* 11% volume fraction ($\Delta E_Q = 2.659$ mm s^{-1}) may be assigned as either the thermally trapped hs form of [**2**(MeCN)]$(OTf)_2$, or as [**2**(OTf)](OTf) formed by thermal ligand exchange in the solid.

The latter process is undoubtedly active at elevated temperature, where it is very efficient: thermal treatment of [**2**(MeCN)]$(OTf)_2$ at $T = 350$ K for three days under reduced pressure ($p \approx 10$ mbar) leads to an almost complete loss of the spectral features of the ls complex (Fig. 4c). The main component (volume fraction >80%) of the spectrum obtained at $T \approx 100$ K from the thermally-treated sample shows signatures typical of hs iron(II) complexes ($\delta = 1.097$ mm s^{-1}; ΔE_Q = 2.069 mm s^{-1}). For comparison, a similarly obtained spectrum for the thermally treated sample of [**2**(OTf)](OTf) is shown in Fig. 4d. The spectral appearance and the fit parameters of both thermally treated samples are virtually indistinguishable from the data recorded for native [**2**(OTf)](OTf) (Fig. 4b). That is, the substitution of coordinated triflate by MeCN, operative in MeCN solutions of [**2**(OTf)](OTf), is reversed by thermal treatment of solid [**2**(MeCN)]$(OTf)_2$. We note that DFT-derived isomer shifts are in close agreement (data in square brackets in Table 4) with the experimental data.

In agreement with an irreversible spin state change attendant on ligand exchange in the lattice at elevated temperature, SQUID magnetometry between $4\text{ K} < T < 390$ K (Fig. S6‡) identifies a thermally driven gradual increase of the effective magnetic moment μ_{eff} to > 5.2 μ_B. As is typical for high-spin $3d^6$ transition metal ions, the observed effective magnetic moment is slightly larger than the expected $S = 2$ spin-only value of $\mu_{\text{eff}} = 4.9$ μ_B, due to spin–orbit interactions and contributions of low-lying orbital states.[43] The turnover temperature $T_{1/2} \approx$

Table 4 Mössbauer parameters with focus on the main components of the experimental spectra measured at $T \approx 100$ K[a]

		Volume fraction [%]	δ^b [mm s^{-1}]	ΔE_Q [mm s^{-1}]	Γ_{HWHM} [mm s^{-1}]
$[\mathbf{1}(\mathrm{MeCN})](\mathrm{OTf})_2$	(1)	16.1	1.220(19)	2.909(43)	0.224(35)
	(2)	79.5	1.066(5)	2.112(11)	0.254(9)
mer-$[\mathbf{1}(\mathrm{MeCN})]^{2+}$ ($S = 2$)[c]			[1.00]	[3.56]	
fac-$[\mathbf{1}(\mathrm{MeCN})]^{2+}$ ($S = 2$)[c]			[0.99]	[2.66]	
$[\mathbf{1}(\mathrm{OTf})](\mathrm{OTf})$	(1)	58.7	1.098(6)	3.110(18)	0.199(12)
	(2)	23.5	1.138(15)	2.335(52)	0.215(35)
mer-$[\mathbf{1}(\mathrm{OTf})]^{+}$ ($S = 2$)[c]			[1.01]	[3.36]	
fac-$[\mathbf{1}(\mathrm{OTf})]^{+}$ ($S = 2$)[c]			[1.02]	[2.71]	
$[\mathbf{2}(\mathrm{MeCN})](\mathrm{OTf})_2$		84.7	0.520(1)	0.353(2)	0.145(2)
$[\mathbf{2}(\mathrm{MeCN})]^{2+}$; $S = 0$[c]			[0.61]	[0.46]	
$[\mathbf{2}(\mathrm{OTf})](\mathrm{OTf})$		82.1	1.088(3)	2.123(7)	0.176(5)
$[\mathbf{2}(\mathrm{OTf})]^{+}$ ($S = 2$)[c]			[1.00]	[3.53]	
$[\mathbf{2}(\mathrm{OTf})]^{+}$; $S = 0$[c]			[0.77]	[1.16]	
$[\mathbf{2}(\mathrm{MeCN})](\mathrm{OTf})_2$[d]		82.6	1.097(2)	2.069(4)	0.196(3)
$[\mathbf{2}(\mathrm{OTf})](\mathrm{OTf})$[e]		72.2	1.076(3)	2.033(6)	0.158(4)

[a] The complete set of Mössbauer parameters and the results of measurements obtained at supplementary temperatures are given in Table S4. [b] Isomer shift δ is specified relative to metallic iron at room temperature. [c] Data in square brackets from DFT computation (B3LYP; see Computational Details) of the respective complex cations. [d] After tempering $[\mathbf{2}(\mathrm{MeCN})](\mathrm{OTf})_2$ at $T = 350$ K for three days under reduced pressure. [e] After tempering $[\mathbf{2}(\mathrm{OTf})](\mathrm{OTf})$ at $T = 350$ K for four days under reduced pressure.

320 K is in fair agreement with the value of $T_{1/2} \approx 310$ K obtained by VT-UV/Vis spectroscopy in solution. Notably, the spin-state change of $[\mathbf{2}(\mathrm{MeCN})]^{2+}$, which is reversible in MeCN solution, is found to be irreversible in the solid state.

Competing ligand conformations. As discussed above, the topologies of complexes $[\mathbf{1}(\mathrm{X})]^{n+}$ and $[\mathbf{2}(\mathrm{X})]^{n+}$ in the solid-state structures agree with the sketches in Scheme 1. They also agree with the structural characteristics reported for iron(II) complexes of the closely related ligand Bn-TPEN.[30] That is, in all iron(II) complexes under study, the sixth coordination site is *trans* to one of the tertiary amine donors. The three pyridine donors are arranged in meridional fashion (*mer*-py$_3$). The same holds for the nickel(II) complex salt $[\mathrm{NiL}^2(\mathrm{OH}_2)](\mathrm{ClO}_4)_2$ of the open-chain ligand L^2 (see Fig. 1), which was synthesised for structural comparison.

X-ray crystallography reveals, however, a different situation in the nickel(II) complex $[\mathrm{NiL}^1(\mathrm{ClO}_4)](\mathrm{ClO}_4)$ of the constrained ligand L^1 (Fig. 1; Table S2‡). Here, the ligand adopts a topology with all three pyridine donors in a facial arrangement (*fac*-py$_3$). This causes the sixth coordination site to be *trans* to one of the pyridine donors. Obviously, ligand L^1 is flexible enough to realise two distinctly different arrangements of its donor atoms in the solid state.

This raises the question whether the preference of the iron(II) complexes for the *mer* conformation in the solid state is conserved for the isolated complex ions $[\mathbf{1}(\mathrm{X})]^{n+}$ and $[\mathbf{2}(\mathrm{X})]^{n+}$ in solution (Scheme 3). Although we have no definite experimental proof of a conformational equilibrium we will, in the following, discuss results from experiment and theory indicating conformational dynamics in the case of $[\mathbf{1}(\mathrm{X})]^{n+}$.

Stereochemical dynamics of a compound, if compatible with the method's timescale, may be studied with NMR techniques. As discussed above, both complexes, $[\mathbf{1}(\mathrm{X})]^{n+}$ and $[\mathbf{2}(\mathrm{X})]^{n+}$, give rise to paramagnetically shifted resonances at room temperature (Table 2). The number of individual resonances, pertinent to $[\mathbf{1}(\mathrm{X})]^{n+}$ and $[\mathbf{2}(\mathrm{X})]^{n+}$, however, is strikingly different (Fig. S5‡). Eighteen individual resonances (accounting for 28 of the total 29 protons) can be unambiguously resolved in the spectrum of $[\mathbf{2}(\mathrm{OTf})](\mathrm{OTf})$ in dichloromethane at room temperature (similar observations apply to $[\mathbf{2}(\mathrm{MeCN})](\mathrm{OTf})_2$ in MeCN), indicating that an asymmetric structure of the hs complexes persists in solution. Individual resonances of all of the aromatic protons are resolved in the low-temperature spectra of $[\mathbf{2}(\mathrm{MeCN})](\mathrm{OTf})_2$ in MeCN and leave no doubt that asymmetry applies also to its diamagnetic ls form.

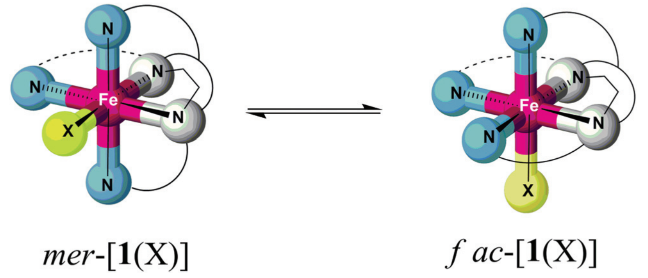

Scheme 3 Presumed stereodynamic exchange between geometrical isomers of $[\mathbf{1}(\mathrm{X})]^{n+}$ in solution.

By contrast, only ten individual resonances can be detected for complexes of ligand L^1. This finding is incommensurate with a (static) asymmetric structure of $[\mathbf{1}(\mathrm{X})]^{n+}$ in solution. We suggest that the apparent symmetry is due to fast stereochemical dynamics within the ligand L^1 of $[\mathbf{1}(\mathrm{X})]^{n+}$, giving rise to spectral averaging of different conformers of the complex (Scheme 3).

DFT computations of relevant complex ions containing L^1 and L^2 were performed to gain insight into the energetics of the anticipated conformational equilibrium (Table 5; *cf.* Table S3‡ for structural data). In the case of ligand L^2,

Table 5 Relative electronic energies (in kJ mol^{-1}) of *mer* and *fac* conformers of iron(II) precursors $[\mathbf{1}(X)]^{n+}$ and $[\mathbf{2}(X)]^{n+}$ (from DFT calculations)[a]

	mer	*fac*
$[\mathbf{1}(OTf)]^+$	0	+10.1 (+4.4)
$[\mathbf{1}(MeCN)]^{2+}$	0	+4.5 (+4.0)
$[\mathbf{2}(OTf)]^+$	0	+26.2 (+21.6)
$[\mathbf{2}(MeCN)]^{2+}$	0	+22.6 (+22.9)

[a] Fully optimised structures at B3LYP-D3/def2-TZVP level. Quintet state (S = 2). In parentheses: with COSMO solvent model (MeCN).

optimisation of the structures of $[\mathbf{2}(X)]^{n+}$ (with X = OTf^-, MeCN) clearly points to a preference for the *mer* conformation in solution. In contrast, energy differences ΔE_{conf} between the isomers of $[\mathbf{1}(X)]^{n+}$ remain below 5 kJ mol^{-1}, which means that, for complexes of ligand L^1, a conformational equilibrium in solution must be taken into account.

In order to test the hypothesis of competing ligand conformations, powder samples have been prepared from solutions of [**1**(OTf)](OTf) in acetonitrile and dichloromethane by rapid precipitation. As shown above for the complexes of ligand L^2, these samples mirror the constitution of the complex in solution; that is, precipitation occurs without significant ligand scrambling. It was thus assumed that rapid precipitation can also "freeze out" conformational dynamics, such that the solid samples will depict also the conformational equilibrium of the complexes $[\mathbf{1}(X)]^{n+}$. If this was actually the case, each conformer must contribute to the Mössbauer spectra individually; that is, two hs components will be visible.

Powder samples of $[\mathbf{1}(MeCN)](OTf)_2$ and [**1**(OTf)](OTf) actually give Mössbauer spectra typical of hs iron(II) complexes (spectra at $T \approx 100$ K in Fig. 5; fit parameters of the main components in Table 4). Importantly, the spectra are clearly dominated by two close-lying hs doublets at all temperatures studied (minor impurity signals are observed). We assign this pattern to conformers of the complexes; an assignment of the spectral components to specific complex conformers, *i.e.*, *mer vs. fac*, is not attempted.

The nature of the co-ligand, MeCN or OTf, significantly affects the appearance of the spectra, with respect to quadrupole splitting and volume fraction. In particular, the quadrupole splitting ΔE_Q of [**1**(OTf)](OTf) is temperature-dependent. Between T = 20 K and 200 K, the quadrupole splitting decreases by *ca.* 1 mm s^{-1} with increasing temperature, whereas the quadrupole splitting of $[\mathbf{1}(MeCN)](OTf)_2$ is almost invariant with temperature (*cf.*, Table S4‡). In principle, several sources may contribute to the thermal effect on ΔE_Q,[44,45] *e.g.* concerning the thermal population of the ligand-field multiplets, the presence of spin–orbit interactions, or molecule dynamics (*e.g.*, rotation or vibration of the molecule or parts of it), which then (partially) average out the effective electric field gradient at the ^{57}Fe nucleus site. In the latter case, hindered molecule dynamics disfavours the averaging process at lower temperature. In view of the observed significant crystallographic disorder involving position, conformation and bond distances of coordinated triflate in [**1**(OTf)](OTf) (see Table 1), we suggest that, at high temperature, stereodynamic mobility of the coordinated triflate ion allows thermal exchange among different rotamers; a process that is frozen out or locked at lower temperature. Consistent with this interpretation, quadrupole splitting at $T \approx 200$ K of the spectral components of [**1**(OTf)](OTf) is indistinguishable from the splitting of $[\mathbf{1}(MeCN)](OTf)_2$, but deviates massively at lower temperature.

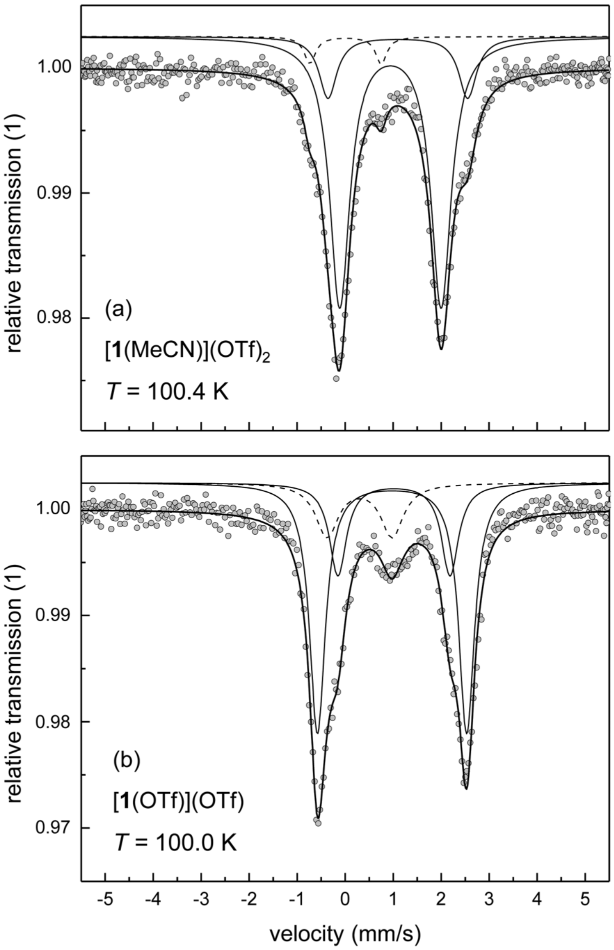

Fig. 5 Mössbauer spectra at $T \approx 100$ K of powder samples obtained by precipitation from solutions of [**1**(OTf)](OTf) (Symbols: experimental data; lines: fit; for clarity the sub-spectra are plotted with an offset against the y axis): (a) $[\mathbf{1}(MeCN)](OTf)_2$ from MeCN solution; (b) [**1**(OTf)]-(OTf) from dichloromethane solution.

Quantitative analysis of the volume fractions of the two main components in the spectrum of [**1**(OTf)](OTf) reveals an apparent temperature dependence. While the main components contribute with *ca.* 59% and 24% at T = 100 K, these components contribute equally with *ca.* 42% and 49% at T = 20 K (*cf.* Table S4‡). We note that, at the same time, the volume fraction of an impurity phase decreases significantly from 18% at T = 100 K to 9% at T = 20 K. These spectral changes are not associated with temperature effects on speciation and/or spin state of the compound, but are artefacts of

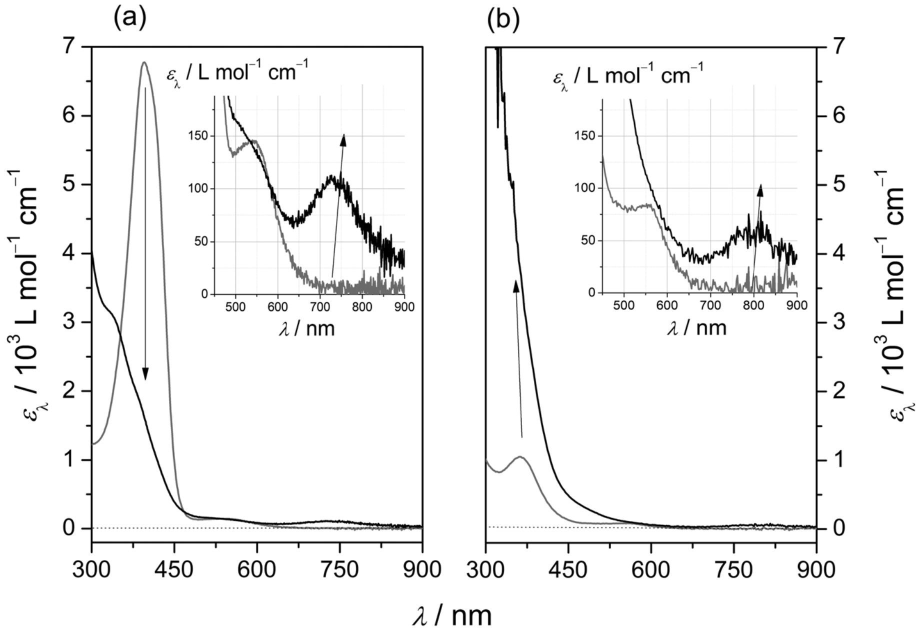

Fig. 6 UV/Vis spectra of iron(II) precursor solutions in acetonitrile before (grey) and after reaction with one equivalent of *m*CPBA (black); (a) [**2**(OTf)](OTf) (c_{Fe} = 2 × 10^{-4} mol L^{-1}; *T* = 293 K; light path *d* = 1.0 cm) at *t* = 0 s and *t* = 1000 s; (b) [**1**(OTf)](OTf) (c_{Fe} = 5 × 10^{-3} mol L^{-1}; *T* = 233 K; light path *d* = 0.1 cm) at *t* = 0 s and *t* = 2 s; insets: spectral region diagnostic of oxoiron(IV) species; apparent molar absorption coefficients ε_λ are normalised with respect to the total amount of iron.

spectral fitting, due to spectral cross-talk among the components associated either with [**1**(OTf)](OTf) or the impurity phase. The overall phenomenology reflects the difference in Lamb-Mössbauer factors (and Debye temperatures in the framework of a simple Debye model) of complex and impurity. Between *T* = 20 K and 200 K, the total spectral area of the related doublets was found to vary by a factor of 5.2 in the case of [**1**(OTf)](OTf), but only by a factor of 1.2 in the case of the impurity phase. Thus, the Lamb-Mössbauer factor of [**1**(OTf)](OTf) increases significantly with decreasing temperature, whereas the Lamb-Mössbauer factor of the impurity barely varies with temperature. In consequence, only the Mössbauer data at low temperature, *i.e.*, at *T* = 20 K give reliable volume fractions that may be associated with different ligand conformations.

Formation of oxoiron(IV) complexes of L^1 and L^2

As a consequence of ligand-imposed distortion of the coordination sphere, the structures, coordination isomers, and spin states of the iron(II) complexes $[\mathbf{1}(X)]^{n+}$ and $[\mathbf{2}(X)]^{n+}$ differ distinctly. Our preliminary work presented here addresses the question whether these differences affect the formation and reactivity of oxoiron(IV) complexes derived from these precursors. We find that formation kinetics, spectroscopic signature and reactivity of oxoiron(IV) complexes thus obtained are strongly affected by the degree of distortion in the ligand fields as supplied by ligands L^1 and L^2.

$$[\mathrm{Fe^{II}L}^n(\mathrm{MeCN})]^{2+} + m\mathrm{CPBA} \rightarrow [\mathrm{L}^n\mathrm{Fe^{IV}{=}O}]^{2+} + m\mathrm{CBA} \qquad (2)$$

Oxoiron(IV) complexes of both ligands, L^1 and L^2, are accessible in moderate yields by reaction of their iron(II) precursors with equimolar amounts of *meta*-chloroperbenzoic acid (*m*CPBA) according to eqn (2). The assignment of the oxoiron(IV) complexes relies on *in situ* UV/Vis spectroscopic methods and *ex situ* mass spectrometric analysis, as the limited lifetimes of the metastable products interfered with their isolation and bulk chemical analysis.

Reactions of dilute solutions (0.1 mmol L^{-1} < [Fe] < 5 mmol L^{-1}) of the iron(II) precursors [**1**(OTf)](OTf) and [**2**(OTf)](OTf) in acetonitrile with equimolar amounts of *m*CPBA proceed with characteristic UV/Vis-spectroscopic response (Fig. 6; data in Table 6). In both cases, diagnostic absorption bands at λ = 810 nm and λ = 730 nm are recorded in the visible spectral region, for $[\mathbf{1}(O)]^{2+}$ and $[\mathbf{2}(O)]^{2+}$, respectively. It is noted that in the case of $[\mathbf{1}(O)]^{2+}$ (Fig. 6, right panel) measurements had to be performed at *T* = 233 K, due to the high intrinsic reactivity of the oxoiron(IV) species at room temperature. While the peak positions of these absorption bands agree with values reported

Table 6 Spectroscopic features of oxoiron(IV) complexes of L^1 and L^2 and time domains of their formation and decay

	T/K	λ_{max}/nm (ε/cm^{-1} L mol^{-1}) [a]	t_{form}/s	$t_{1/2}$/s
$[\mathbf{1}(O)]^{2+}$	233	810 (>80)	<2	>10^3
$[\mathbf{2}(O)]^{2+}$	293	730 (>150)	≈10^3	>10^5

[a] Apparent molar absorption coefficient, normalised to iron content.

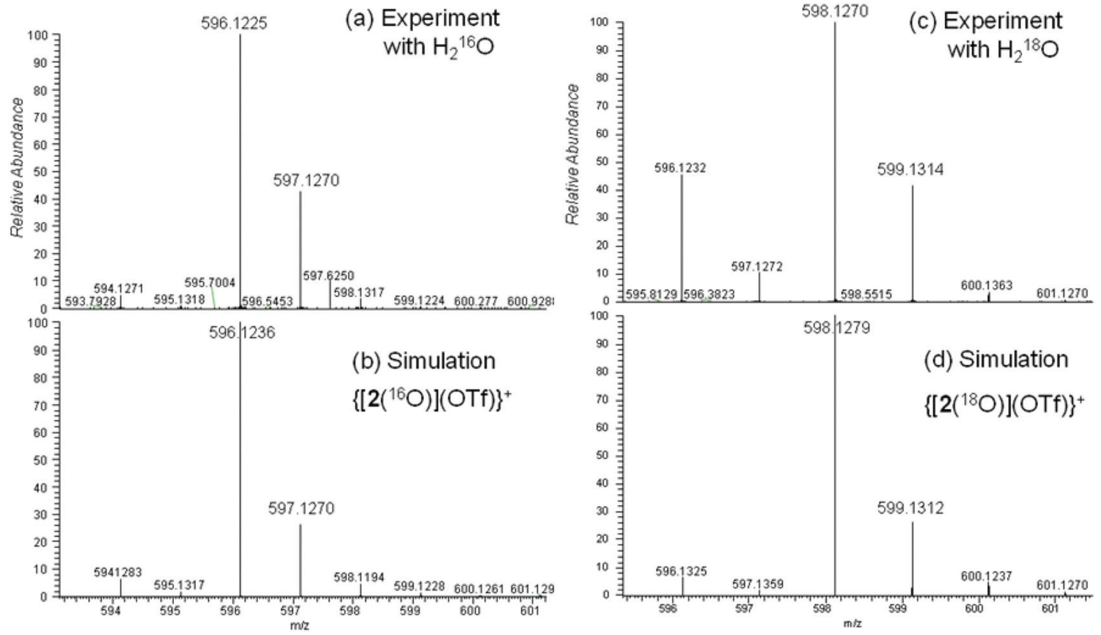

Fig. 7 Mass-spectrometric analysis of equimolar mixtures of [**2**(MeCN)](OTf)$_2$ and PhIO in MeCN; (a) reaction in the presence of H$_2$^{16}O; (c) reaction in the presence of an excess of H$_2$^{18}O; (b) and (d) show simulations of the experimental data.

for other oxoiron(IV) species, the molar absorption coefficients are somewhat smaller than the majority of published values.[10] Although we cannot rule out intrinsically small values, we assume sub-stoichiometric formation of the oxoiron(IV) species.

Further arguments in favour of our assignment derive from ESI mass-spectrometric (ESI-MS) analysis of acetonitrile solutions of [**2**(OTf)](OTf) after reaction with iodosobenzene, PhIO. Formal addition of one oxygen atom to the complex fragment [Fe(L^2)] ([**2**]) is indicated by diagnostic signals in the mass spectra. Dominant signals (50%) at m/z = 596.1226 (calc. for [$C_{24}H_{29}N_5FeO_4F_3S$]$^+$: m/z = 596.1236) are assigned to {[**2**(O)]-(OTf)}$^+$ (Fig. 7a and b). Weak signals at m/z = 223.5856 (calc. for [$C_{23}H_{29}N_5FeO$]$^{2+}$: m/z = 223.5855) indicate small amounts of native [**2**(O)]$^{2+}$. Experiments in the presence of $^{18}OH_2$ gave strong signals (60%) at m/z = 598.1268 (calc. for [$C_{24}H_{29}N_5Fe^{18}O^{16}O_3F_3S$]$^+$: m/z = 598.1279) (Fig. 7c and d). Weak signals at m/z = 224.5875 (calc. for [$C_{23}H_{29}N_5Fe^{18}O$]$^{2+}$: m/z = 224.5877) are indicative of native [**2**(^{18}O)]$^{2+}$. The signals show that speciation is consistent, but they also highlight the presence of ^{18}O in the oxidation products of interest. This suggests isotope exchange between $^{18}OH_2$ and the product of the *m*CPBA-induced oxidation reaction, providing conclusive evidence for the formation of an oxoiron(IV) complex of ligand L^2.[46]

Mass-spectrometric analysis failed to provide direct evidence for the formation of the corresponding oxoiron(IV) complex of ligand L^1. This failure is probably due to the complex's high intrinsic reactivity: the UV/Vis spectra recorded directly after mixing the reactants at room temperature have no feature attributable to an oxoiron(IV) species; rather, they are assignable to the products of the latter's rapid intramolecular decay. Current work seeks to clarify the decay pathway.

Differences in the long-wavelength absorption maxima of both oxoiron(IV) species reflect their diverging electronic properties. In particular, the oxoiron(IV) complex of the constrained ligand L^1 exhibits a ligand-field strength significantly weaker than that of its less-strained congener. The difference of *ca.* 100 nm in the positions of their long-wavelength d → d absorption bands translates into a difference in the excitation energy of *ca.* 20 kJ mol^{-1}. We note that this ligand-imposed energy difference ties in nicely with the DFT-derived ligand-imposed differences in ligand-field splitting (Table 3).

Differences between the complexes also extend to the formation kinetics. In the case of ligand L^1, the growth of the characteristic long-wavelength band at 810 nm is limited by the mixing time of the substrates ($t_{mix} \approx 2$ s). Growth is already complete by the time the first reaction spectrum is recorded. This behaviour is quite remarkable, as these experiments were performed at low temperature (T = 233 K), pointing to a very labile iron(II) precursor. These indications of a labile ligand sphere and a weakened ligand field in the case of the oxoiron(IV) species of L^1 are both in line with our "distortion hypothesis". Accordingly, the less distorted iron(II) precursor, of ligand L^2, forms the oxoiron(IV) species much more slowly, completing the reaction after *ca.* 15 minutes at ambient temperature.

Conclusions

In the present work, we have established incremental ligand-field distortion as a tool to tune the structural, conformational and spin-state preferences of iron(II) complexes, in ligand fields set up by two pentadentate N_5 ligands. Within our pair of ligands (diazepane-based L^1; open chain L^2), the donor-atom inherent strength of the donor set (diamine/trisimine) is fully conserved. Accordingly, solely the consequences of ligand sphere distortion are recorded in complexes of the type $[\mathrm{FeL}^n(\mathrm{X})]\mathrm{Y}$, in isolation from effects caused by a variation of the donor set.

The decisive structural distinction between the ligands is introduced as an angular constraint of the diamine unit, by forcing it into a diazepane ring in L^1, thereby enhancing the *trans* effect of the co-ligand X. The combination of both aspects translates into massive radial disorder and renders the coordination sphere intermediate between tetragonal and trigonal symmetry. Our combined experimental and quantum-chemical findings show that ligand-field imposed differences are the root cause of the differences in properties observed for the iron(II) complexes of L^1 and L^2. Ligand-imposed distortion in L^1 reduces the ligand-field strength by *ca.* 20–30 kJ mol^{-1} and, thus, places this factor on an equal footing with ligand-field effects due to variation in the co-ligand. Destabilisation of the ligand field translates into a marked preference of the constrained ligand L^1 for high-spin complexes and into high kinetic lability of the derived iron(II) complexes.

Preliminary results, obtained after reacting the iron(II) complexes $[\mathrm{FeL}^n(\mathrm{X})]\mathrm{Y}$ with *meta*-chloroperbenzoic acid, indicate that the influence of ligand-imposed distortion of L^n is traceable also in the properties of the resulting oxoiron(IV) complexes. Oxoiron(IV) species of L^1 and L^2 are identified through their diagnostic UV/Vis absorption spectra and by mass-spectrometric results (L^2). Significantly reduced ligand-field strength is accompanied by high intrinsic reactivity in the case of L^1. Current work addresses the question to what extent judiciously chosen substituents on L^1 and L^2 allow additional modulation of oxoiron(IV) reactivity.

Experimental section

Materials and general procedure

All reagents and solvents were purchased from commercial sources (Sigma-Aldrich, Acros). Reagents were used as received, and solvents dried according to published procedures.[47] The synthesis of the constrained ligand L^1 and of its complexes $[\mathrm{FeL}^1(\mathrm{Cl})](\mathrm{PF_6})$ ($\equiv [\mathbf{1}(\mathrm{Cl})](\mathrm{PF_6})$) and $[\mathrm{FeL}^1(\mathrm{Br})](\mathrm{PF_6})$ ($\equiv [\mathbf{1}(\mathrm{Br})](\mathrm{PF_6})$) has been described previously.[29]

UV/Vis spectroscopy

UV/Vis spectra at ambient temperature were measured with a Varian Cary 50 spectrometer through quartz cells (light path d = 1 cm). Sample concentration was in the range of 10^{-4} mol L^{-1}. For variable-temperature experiments, a UV/Vis quartz immersion probe (light path d = 1 mm, Hellma) with a home-built measuring cell came to use. Sample concentration was in the range of 10^{-3} mol L^{-1} in this case. Temperature was controlled by an immersion thermometer.

Mössbauer spectroscopy

^{57}Fe-Mössbauer spectroscopic measurements have been performed on a conventional transmission spectrometer with sinusoidal velocity sweep. The activity of the Mössbauer source was about 40 mCi of ^{57}Co in a rhodium matrix kept at room temperature. The measurements were done with a CryoVac continuous flow cryostat with N_2 or Helium exchange gas. The temperature was measured with a calibrated Si diode located close to the sample container. The isomer shift δ is specified relative to metallic iron at room temperature and was not corrected for second order Doppler shift. The measurements on $[\mathbf{1}(\mathrm{OTf})](\mathrm{OTf})$ were carried out with a Janis closed-cycle cryostat with comparable specifications, geometry and sample environments as described above. The activity of the Mössbauer source used here was about 10 mCi of ^{57}Co in a rhodium matrix.

SQUID magnetometry

SQUID magnetometry measurements were performed on a Cryogenic Ltd. closed-cycle SQUID magnetometer. The sample was weighed in a gelatin capsule and then fixed in a polyethene sample holder. The background signal of the empty gelatin capsule and the sample holder were experimentally determined and subtracted from the experimental raw data set. The correction of the diamagnetic susceptibility of the complex was done by use of tabulated Pascal parameters.

X-ray data collection and refinement details

Data were collected at 150.00(10) K using an "Oxford Diffraction Xcalibur S" diffractometer equipped with a goniometer in κ geometry, a "Sapphire 3" CCD-detector, and a graphite-monochromated "Enhance" Mo-K_α source (λ = 0.71073 Å) or an "Agilent Nova" diffractometer equipped with a goniometer in κ geometry, an "Atlas" CCD-detector, and a mirror-monochromated "SuperNova" Cu-K_α source (λ = 1.54184 Å). Diffraction images were integrated with CrysAlisPro. An empirical absorption correction using spherical harmonics implemented in the Scale3 AbsPack scaling algorithm was performed.[48] Structures were solved iteratively with Superflip[49] (for $[\mathbf{1}(\mathrm{OTf})](\mathrm{OTf})$, $[\mathbf{2}(\mathrm{Cl})](\mathrm{PF_6})\cdot\frac{1}{4}\mathrm{Et_2O}$, and $[\mathrm{Ni}\mathbf{L^2}(\mathrm{H_2O})](\mathrm{ClO_4})_2\cdot\mathrm{MeOH}$) or with SHELXS-97 using direct methods (for $[\mathbf{1}(\mathrm{CH_3CN})](\mathrm{BPh_3})_2$, $[\mathbf{2}(\mathrm{OTf})](\mathrm{OTf})$, and $[\mathrm{Ni}\mathbf{L^1}(\mathrm{ClO_4})](\mathrm{ClO_4})\cdot\mathrm{MeOH}$) and refined with SHELXL-97[50] against $F_o{}^2$ data using the full-matrix least-squares algorithm. Non-hydrogen atoms were refined anisotropically; hydrogen atoms were refined isotropically with standard riding-models. Molecular graphics were produced using Mercury.[51] Crystallographic details are summarised in Table S1.‡

All disordered parts of the crystal structures were modelled in two discrete positions using (tight) rigid-bond and isotropy restraints. For the triflato ligand in $[\mathbf{1}(\mathrm{OTf})](\mathrm{OTf})$, the occupancies refined to 0.51(2)/0.49(2). In $[\mathrm{Ni}\mathbf{L^1}(\mathrm{ClO_4})](\mathrm{ClO_4})\cdot\mathrm{MeOH}$, the perchlorate ion containing Cl2 was modelled using additional same-distance restraints for the oxygen atoms; occupancies refined to 0.57(3)/0.43(3). In $[\mathbf{2}(\mathrm{OTf})](\mathrm{OTf})$, the triflato ligand is rotationally disordered about the O40–S43 axis.

Using additional same-distance restraints with standard weights for the whole ligand, occupancies refined to 0.52(3)/0.48(3). The unit cell of $[\mathbf{2}(Cl)](PF_6)\cdot\frac{1}{4}Et_2O$ contains half a very strongly disordered diethyl-ether molecule that had to be treated as a diffuse contribution to the overall scattering without specific atom positions by Squeeze/Platon.[52] In $[Ni\mathbf{L}^2(H_2O)](ClO_4)_2\cdot MeOH$, the hydrogen atoms of the aqua ligand were located on a Fourier difference map and refined semi-freely. The perchlorate ion containing Cl2 exhibits rotational disorder along the O6–Cl2 axis. Occupancies refined to 0.716(9)/0.284(9). The Cl–O distances were restrained to be equal and refined to an average of 1.427(7) Å. The Flack parameter refined to $x = 0.005(12)$, thus supporting enantiopurity of the crystal and the correct assignment of absolute structure.[53]

Synthesis of ligand L^2

1,3,5-Trimethyl-5-(2-pyridinyl)-hexahydropyrimidine (A).

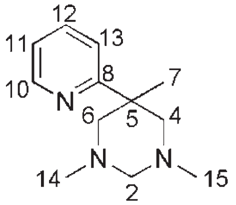

A solution of 2-methyl-2-(2-pyridyl)-propane-1,3-diamine[32] (2.06 g; 12.5 mmol) in MeOH (150 ml) is stirred with *para*-formaldehyde (1.31 g; 39.3 mmol) for 12 h at ambient temperature. To the cooled mixture (0 °C) $NaBH_4$ (5.65 g; 149.3 mmol) is added as a solid in portions within 1 h. The mixture is allowed to warm to ambient temperature within 16 h. After addition of a few drops of acetic acid, the volatiles are removed under reduced pressure. A solution of the solid residue in water (200 ml) was treated with NaOH and extracted with $CHCl_3$ (3 × 200 ml). From the combined organic phases, the product is obtained as a colourless oil after removing the solvent *in vacuo* (yield: 2.51 g; 98%). **^{1}H-NMR** (200 MHz, $CDCl_3$, 25 °C): δ [ppm] = 8.51 (ddd, 1H, $^3J_{H,H}$ = 5.5 Hz, $^4J_{H,H}$ = 2.0 Hz, $^5J_{H,H}$ = 1.0 Hz, H^{10}), 7.56 (dt, 1H, $^3J_{H,H}$ = 8.0 Hz, $^4J_{H,H}$ = 2.0 Hz, H^{12}), 7.36 (td, 1H, $^3J_{H,H}$ = 8.0 Hz, $^4J_{H,H}$ = 1.3 Hz, H^{13}), 7.03 (ddd, 1H, $^3J_{H,H}$ = 8.0 Hz, $^3J_{H,H}$ = 5.5 Hz, $^4J_{H,H}$ = 1.5 Hz, H^{11}), 3.39 (d, 2H, H^{5,7}), 3.42–2.11 (brm, 6H, H^{2,4,6}), 2.18 (s, 6H, H^{14,15}), 1.26 (brs, 3H, H^7); **HR-MS** (ESI): Calcd for $C_{12}H_{19}N_3$: $[M + H]^+$ 206.1652; found. $[M + H]^+$ 206.1651.

N^1,N^3,2-Trimethyl-2-(pyridin-2-yl)propane-1,3-diamine (B).

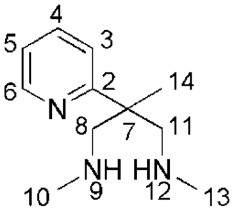

The aminal **A** (2.35 g; 11.42 mmol) is dissolved in technical 1,2-ethanediol (70 ml). After addition of HCl (32%; 150 ml) the mixture is stirred for 8 days at 55 °C. From 25 ml aliquots of the cooled mixture (0° C), the amine is deliberated by addition of 1,2-ethylendiamine (15 ml; exothermic reaction; temperature below 30 °C). The combined alkaline mixtures are diluted with water and extracted with three portions of $CHCl_3$. After evaporation of all volatiles the residue is extracted with pentane (6 × 5 ml) and the volume of the combined pentane phases reduced to 10 ml. The pentane solutione is extracted with a concentrated $NaHCO_3$ solution (3 × 10 ml). The combined aqueous phases are extracted with $CHCl_3$ (3 × 10 ml). After evaporation of the combined organic phases under reduced pressure, the secondary amine **B** is obtained as a yellow oil (yield: 1.18 g; 53%). **^{1}H-NMR** (200 MHz, $CDCl_3$, 25 °C): δ [ppm] = 8.55 (ddd, 1H, $^3J_{H,H}$ = 5.5 Hz, $^4J_{H,H}$ = 2.0 Hz, $^5J_{H,H}$ = 1.0 Hz, H^6), 7.63 (dt, 1H, $^3J_{H,H}$ = 8.0 Hz, $^4J_{H,H}$ = 2.0 Hz, H^4), 7.35 (td, 1H, $^3J_{H,H}$ = 8.0 Hz, $^4J_{H,H}$ = 1.3 Hz, H^3), 7.10 (ddd, 1H, $^3J_{H,H}$ = 8.0 Hz, $^3J_{H,H}$ = 5.5 Hz, $^4J_{H,H}$ = 1.5 Hz, H^5), 2.96 (d, 2H, $^2J_{H,H}$ = 12 Hz, H^{8,11}), 2.88 (d, 2H, $^2J_{H,H}$ = 12 Hz, H^{8,11}), 2.38 (s, 6H, H^{10,13}), 1.98 (brs, 2H, H^{9,12}), 1.39 (s, 3H, H^{14}), **HR-MS** (ESI): Calcd for $C_{23}H_{27}N_5$: $[M + H]^+$ 374.2339; found. $[M + H]^+$ 374.2336.

N^1,$N^{3,2}$-Trimethyl-2-(pyridin-2-yl)-N^1,N^3-bis(pyridin-2-ylmethyl)-propan-1,3-diamin (L^2).

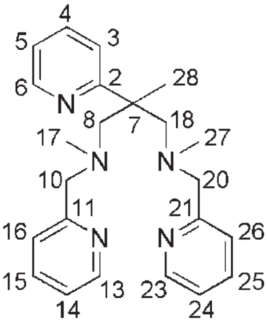

A mixture of the secondary amine **B** (0.55 g; 2.8 mmol) with Na_2CO_3 (3.03 g; 28.6 mmol) and 2-picolylchloride-hydrochloride (0.94 g; 5.7 mmol) in acetonitrile is stirred at 55 °C for two days. After cooling to ambient temperature, the solvent is removed under reduced pressure. The red oil obtained is dissolved in toluene and the resulting solution extracted with water. Toluene is removed under reduced pressure and the residue is extracted several times with pentane. From the combined pentane extracts, ligand **L^2** is obtained as a yellow oil after removing all volatiles *in vacuo* (yield: 0.67 g; 63%). **^{1}H-NMR** (200 MHz, $CDCl_3$, 25 °C): δ [ppm] = 8.50 (ddd, 1H, $^3J_{H,H}$ = 5.5 Hz, $^4J_{H,H}$ = 2.0 Hz, $^5J_{H,H}$ = 1.0 Hz, H^6), 8.40 (ddd, 2H, $^3J_{H,H}$ = 5.5 Hz, $^4J_{H,H}$ = 2.0 Hz, $^5J_{H,H}$ = 1.0 Hz, H^{13,23}), 7.52 (dt, 3H, $^3J_{H,H}$ = 8.0 Hz, $^4J_{H,H}$ = 2.0 Hz, H^{4,15,25}), 7.40 (td, 1H, $^3J_{H,H}$ = 8.0 Hz, $^4J_{H,H}$ = 1.3 Hz, H^3), 7.26 (td, 2H, $^3J_{H,H}$ = 8.0 Hz, $^4J_{H,H}$ = 1.3 Hz, H^{16,26}), 7.04 (ddd, 2H, $^3J_{H,H}$ = 8.0 Hz, $^3J_{H,H}$ = 5.5 Hz, $^4J_{H,H}$ = 1.5 Hz, H^{14,24}), 6.98 (ddd, 1H, $^3J_{H,H}$ = 8.0 Hz, $^3J_{H,H}$ = 5.5 Hz, $^4J_{H,H}$ = 1.5 Hz, H^5), 3.55 (s, 4H, H^{10,20}), 3.06 (d, 2H, $^2J_{H,H}$ = 13 Hz, H^{8,18}), 2.80 (d, 2H, $^2J_{H,H}$ = 13 Hz, H^{8,18}), 2.01 (s, 6H, H^{17,27}), 1.55 (s, 3H, H^{28}). **{^{1}H}^{13}C-NMR** (50.32 MHz, $CDCl_3$, 25 °C): δ [ppm] = 166.2 (C$_q$, 1C, C^2), 160.6 (C$_q$, 2C, C^{11,21}), 148.8 (CH, 2C, C^{13,23}), 148.3 (CH, 1C, C^6), 136.3 (CH, 2C, C^{15,25}), 135.9 (CH, 1C, C^4), 122.7 (CH, 2C, C^{16,26}), 121.9

(CH, 1C, C^3), 121.7 (CH, 2C, $C^{14,24}$), 120.9 (CH, 1C, C^5), 66.9 (CH_2, 2C, $C^{8,18}$), 66.1 (CH_2, 2C, $C^{10,20}$), 48.2 (C_q, C, C^7), 45.0 (CH_3, 3C, $C^{17,27}$), 20.8 (CH_3, 1C, C^{28}). **Combustion analysis**: Calcd (%) for $C_{23}H_{29}N_5$ (375.51): C 73.57, H 7.78, N 18.65; found.: C 73.59, H 7.72, N 18.95. **HR-MS** (ESI): Calcd for $C_{23}H_{29}N_5$: $[M+H]^+$ 376.2496; found $[M+H]^+$ 376.2495.

Synthesis of metal complexes

Iron(II) Triflato complexes: general procedure. After addition of a solution of the ligand in acetonitrile (2 ml) to a suspension of $Fe(OTf)_2$ in acetonitrile (2 ml), the reaction mixture is stirred for 1 d at room temperature. After removing acetonitrile under reduced pressure, dichloromethane was added. The solution was stirred for 1 h and then treated with diethyl ether (20 ml) to give a light yellow solid. This is collected by filtration, washed with diethyl ether, and dried *in vacuo*. Isothermal diffusion of diethyl ether into a solution in dichloromethane affords the product as a yellow crystalline material.

[FeL^1(OTf)](OTf) (≡[1(OTf)](OTf)). (L^1: 0.340 g (0.91 mmol); $Fe(OTf)_2$: 0.31 g (0.86 mmol)). Yield: 0.53 g (84%). $C_{25}H_{27}F_6FeN_5O_6S_2$ (727.48): calcd C 41.28, H 3.74, N 9.63, S 8.82; found C 41.49, H 4.02, N 9.36, S 7.97. **HR-MS (ESI)**: calcd for $C_{24}H_{27}F_3FeN_5O_3S$ $[M]^+$ 578.1124; found 578.1131; calcd for $C_{23}H_{27}FeN_5$ $[M]^{2+}$ 214.5801; found 214.5802; **^{1}H-NMR** (200 MHz, CD_2Cl_2, 23 °C): δ [ppm] = 114.1, 50.9, 48.4, 39.8, 37.5, 34.8, 15.0, 10.3, 6.2, −1.7.

[FeL^2(OTf)](OTf) (≡ [2(OTf)](OTf)). (L^2: 0.360 g (0.95 mmol); $Fe(OTf)_2$: 0.32 g (0.90 mmol)). Yield: 0.57 g (87%). $C_{26}H_{31}Cl_2F_6FeN_5O_6S_2$ (814.43): C 38.34, H 3.84, N 8.60, S 7.87; found C 38.57, H 3.95, N 8.96, S 7.52. **HR-MS (ESI)**: Calcd for $C_{24}H_{29}F_3FeN_5O_3S$ $[M]^+$ 580.1287; found $[M]^+$ 580.1276; calcd for $C_{23}H_{27}FeN_5$: $[M]^{2+}$ 215.5881; found $[M]^{2+}$ 215.5876; **^{1}H-NMR** (200 MHz, CD_2Cl_2, 23 °C): δ [ppm] = 85.5, 64.0, 60.6, 57.3, 52.5, 49.7, 47.5, 44.6, 33.0, 32.4, 29.9, 25.2, 16.0, 12.4, 3.5, 1.5, −0.9.

[FeL^1(MeCN)](BPh$_4$)$_2$ (≡ [1(MeCN)](BPh$_4$)$_2$). After adding a solution of ligand L^1 (0.15 g; 0.40 mmol) in acetonitrile (6 ml) to a solution of $Fe(ClO_4)_2·6H_2O$ (0.131 g; 0.36 mmol) in dried acetonitrile (2 ml), the resulting orange-red mixture is stirred overnight at ambient temperature under an atmosphere of dry N_2. After removing the solvent under reduced pressure, the residue is stirred vigorously with excess diethyl ether. The off-white solid formed is isolated by filtration, washed with diethyl ether and dried *in vacuo*. Yellow crystals of [**1**(ClO_4)](ClO_4) are obtained within one week by layering a solution of the product in acetone with diethyl ether. Metathesis of the counter ion in [**1**(ClO_4)](ClO_4) is achieved by adding an excess of $NaBPh_4$ (4 eq.) to a solution of [**1**(ClO_4)](ClO_4) in methanol. The formed solid is separated by filtration and washed with methanol and diethyl ether. Layering a solution of the solid product in acetonitrile with diethyl ether affords yellowish single crystals of [**1**(CH_3CN)](BPh_4)$_2$ within one week. **^{1}H-NMR** (200 MHz, CD_3CN, 23 °C): δ [ppm] = 92.4, 64.9, 58.7, 50.0, 48.8, 23.1, 17.6, 3.4, −0.9, −5.0.

[FeL^2(Cl)](PF$_6$) (≡[2(Cl)](PF$_6$)). After adding a solution of L^2 (0.125 g; 0.33 mmol) in methanol to a solution of $FeCl_2$ (0.040 g; 0.32 mmol) in methanol, the yellow mixture is stirred for 12 h at ambient temperature. Addition of solid $(nBu)_4NPF_6$ (0.243 g; 0.63 mmol) affords the crude product as a yellow solid. The solid is separated by filtration, washed with diethyl ether and dried *in vacuo*. Isothermal diffusion of diethyl ether into a solution of the product in dichloromethane affords yellow single crystals within several days. Yield: 0.15 g (77%). $C_{23}H_{29}ClF_6FeN_5P$ (611.77): C 45.16, H 4.78, N 11.45; found C 45.61, H 5.08, N 11.24. HR-MS (ESI): Calcd for $C_{23}H_{29}ClFeN_5$: $[M]^+$ 466.1455; found. $[M]^+$ 466.1449.

[FeL^2(MeCN)](OTf)$_2$ (≡[2(MeCN)](OTf)$_2$). A solution of [**2**(OTf)](OTf) in MeCN was stirred at ambient temperature for two hours and then treated with an excess of cold diethyl ether. The obtained powder was separated from solution *via* filtration, washed with cold diethyl ether and dried *in vacuo*.

^{1}H-NMR (400 MHz, CD_3CN, −40 °C): δ [ppm] = 9.68 (bs, 1H), 9.34 (bs, 1H), 8.99 (bs, 1H), 8.10–7.95 (m, 4H), 7.87 (d, 1H, $^3J_{H,H}$ = 7.4 Hz), 7.76 (m, 1H), 7.66 (t, 1H, $^3J_{H,H}$ = 7.6 Hz), 7.54 (m, 1H), 7.49 (d, 1H, $^3J_{H,H}$ = 7.3 Hz), 5.24 (bs, 1H), 4.50 (bs, 2H), 4.10 (m, 2H), 3.37 (m, 2H), 2.81 (s, 3H), 2.19 (s, 3H), 1.50 (s, 3H); **^{1}H-NMR** (400 MHz, CD_3CN, 23 °C): δ [ppm] = 44.1, 30.3, 28.5, 27.0, 23.4, 19.4, 18.7, 16.4, 15.6, 15.2, 13.8, 12.0, 8.6, 7.2, 6.7, 3.6, −0.9.

Nickel(II) complexes: general procedure. After adding a slight excess of ligand L^n as a methanolic solution to a solution of $Ni(ClO_4)_2·6H_2O$ in methanol, the resulting violet mixture is stirred for one day at ambient temperature. Isothermal diffusion of diethyl ether into the solution at ambient temperature affords violet crystalline material within one day. The crystals are separated by filtration, washed with diethyl ether and dried *in vacuo*. **[NiL^1(ClO$_4$)](ClO$_4$).** (L^1: 0.100 g (0.28 mmol); $Ni(ClO_4)_2·6H_2O$ 0.098 g (0.26 mmol). Yield: 0.11 g (82%). $C_{23}H_{27}N_5NiCl_2O_8·MeOH$ (663.13): calcd C 43.47, H 4.71, N 10.56; found C 43.84, H 4.56, N 10.88. HR-MS (ESI): calcd for $C_{23}H_{27}N_5NiClO_4$: $[M]^+$ 530.1100; found 530.1090; calcd for $C_{23}H_{27}N_5Ni$: $[M]^{2+}$ 215.5804; found 215.5802. **[NiL^2(H$_2$O)](ClO$_4$)$_2$.** (L^2: 0.052 g (0.14 mmol); $Ni(ClO_4)_2·6H_2O$ 0.046 g (0.12 mmol). Yield: 0.07 g (84%). $C_{23}H_{29}Cl_2N_5NiO_8$ (633.11): calcd C 43.63, H 4.62, N 11.06; found C 43.91, H 4.83, N 10.99. HR-MS (ESI): calcd for $C_{23}H_{29}N_5NiClO_4$: $[M]^+$ 532.1256; found. $[M]^+$ 532.1250; calcd for $C_{23}H_{29}NiN_5$: $[M]^{2+}$ 216.5883; found $[M]^{2+}$ 216.5881.

Samples of [FeL^n(X)]Y for Mössbauer spectroscopy

Amorphous powder samples of the complexes were obtained by treating solutions of [FeL^n(OTf)](OTf) with an excess of cold diethyl ether. (i) Acetonitrile complexes of L^1 and L^2 with X = MeCN/Y = $(OTf)_2$ from MeCN solutions; (ii) Triflato complexes of L^1 and L^2 with X = Y = OTf^- from MeCN solutions. The obtained powders were separated from solution *via* filtration, washed with cold diethyl ether and dried *in vacuo*. Correct elemental analyses have been obtained in all cases.

Computational details

All DFT and TDDFT calculations were performed using TURBOMOLE6.3[54–59] and a locally modified version of the

TURBOMOLE6.4[56] package. The latter allows variation of the amount of exact exchange in global hybrid functionals. def2-TZVP basis sets[60] were used throughout. The B3LYP[61,62] functional was used (with 20% exact exchange), but for spin-crossover (SCO) energies, B3LYP* (15% exact exchange)[42] has been used, which had been reparameterised to better describe SCO in iron(II) complexes. The SCF energies were converged to 10^{-8} Hartree in energy and a fine m5 grid was chosen. Dispersion contributions were evaluated using Grimme's DFT-D3 atom-pairwise dispersion corrections.[63] In several cases, solvent effects were taken into account at the polarisable continuum model level, using COSMO (Conductor-Like Screening Model)[64] implemented in TURBOMOLE6.3, with permittivity $\varepsilon = 35.688$ for acetonitrile.

For the calculation of Mössbauer parameters, an uncontracted def2-QZVPP basis set was used for iron and def2-TZVP for all other atoms. The structures for the Mössbauer calculations were optimised at B3LYP-D3/def2-TZVP level. The in-house MAG program[65] was used to calculate the electron density ρ at the iron nucleus and the quadrupole splitting. For the isomer shifts the linear equation used is $\delta\ [\mathrm{mm\ s^{-1}}] = -0.3594 \times (\rho(\mathrm{DFT}) - 11\,800) + 10.521$. This equation was fitted to the isomer-shift test of Neese's test set.[66]

Acknowledgements

Dipl.-Chem. S. Kühn (TU Berlin) is acknowledged for assistance with conductivity measurements. Dr M. Schlangen is acknowledged for mass-spectrometric measurements. We acknowledge Prof. Dr. M. Bröring (Institut für Anorganische und Analytische Chemie) and Prof. Dr. F. J. Litterst (Institut für Physik der Kondensierten Materie) at the TU Braunschweig for access to the SQUID magnetometer and ^{57}Fe-Mössbauer equipment. The Deutsche Forschungsgemeinschaft (DFG) is thanked for financial support (grant number GR 1247/7-1 (to A. G.); Berlin excellence cluster UniCat (to M. K.)).

Notes and references

1 B. L. Vallee and R. J. P. Williams, *Proc. Natl. Acad. Sci. U. S. A.*, 1968, **59**, 498.
2 P. Comba, *Coord. Chem. Rev.*, 2000, **200**, 217.
3 K. B. Lipkowitz, S. Schefrick and D. Avnir, *J. Am. Chem. Soc.*, 2001, **123**, 6710.
4 G. Chaka, J. L. Sonnenberg, H. B. Schlegel, M. J. Heeg, G. Jaeger, T. J. Nelson, L. A. Ochrymowycz and D. B. Rorabacher, *J. Am. Chem. Soc.*, 2007, **129**, 5217.
5 V. Balland, C. Hureau and J.-M. Saveant, *Proc. Natl. Acad. Sci. U. S. A.*, 2010, **107**, 17113.
6 A. Hoffmann, S. Binder, A. Jesser, R. Haase, U. Floerke, M. Guida, M. S. Stagni, W. Meyer-Klaucke, B. Lebsanft, L. E. Grünig, S. Schneider, M. Hashemi, A. Goos, A. Wetzel, M. Rubhausen and S. Herres-Pawlis, *Angew. Chem., Int. Ed.*, 2014, **53**, 299.
7 But see: U. Ryde and M. H. M. Olsson, *Int. J. Quantum Chem.*, 2001, **81**, 335.
8 W. Nam, *Acc. Chem. Res.*, 2007, **40**, 522.
9 J. Hohenberger, K. Ray and K. Meyer, *Nat. Commun.*, 2012, **3**, 720.
10 A. R. McDonald and L. Que Jr., *Coord. Chem. Rev.*, 2013, **257**, 414.
11 E. I. Solomon, K. M. Light, L. V. Liu, M. Srnec and S. D. Wong, *Acc. Chem. Res.*, 2013, **46**, 2725.
12 W. Nam, Y.-M. Lee and S. Fukuzumi, *Acc. Chem. Res.*, 2014, **47**, 1146.
13 J. England, Y. Guo, E. R. Farquhar, V. G. Young Jr., E. Münck and L. Que Jr., *J. Am. Chem. Soc.*, 2010, **132**, 8635.
14 Y. M. Lee, S. N. Dhuri, S. C. Sawant, J. Cho, M. Kubo, T. Ogura, S. Fukuzumi and W. Nam, *Angew. Chem., Int. Ed.*, 2009, **48**, 1803.
15 M. Martinho, F. Banse, J.-F. Bartoli, T. A. Mattioli, P. Battioni, O. Horner, S. Bourcier and J.-J. Girerd, *Inorg. Chem.*, 2005, **44**, 9592.
16 J.-U. Rohde, J.-H. In, M. H. Lim, W. W. Brennessel, M. R. Bukowski, A. Stubna, E. Münck, W. Nam and L. Que Jr., *Science*, 2003, **299**, 1037.
17 K. Ray, F. F. Pfaff, B. Wang and W. Nam, *J. Am. Chem. Soc.*, 2014, **136**, 13942.
18 A. R. McDonald, Y. Guo, V. V. Vu, E. L. Bominaar, E. Münck and L. Que Jr., *Chem. Sci.*, 2012, **3**, 1680.
19 Angular overlap model (AOM): C.E. Schäffer and C. K. Jorgensen, *Mol. Phys.*, 1965, **9**, 401.
20 P. Comba, *Coord. Chem. Rev.*, 1999, **182**, 343.
21 E. A. Ünal, D. Wiedemann, J. Seiffert, J. P. Boyd and A. Grohmann, *Tetrahedron Lett.*, 2012, **53**, 54.
22 A. Grohmann, *Dalton Trans.*, 2010, **39**, 1432.
23 D. Wiedemann and A. Grohmann, *Dalton Trans.*, 2014, **43**, 2406.
24 P. Stock, T. Pedzinski, N. Spintig, A. Grohmann and G. Hörner, *Chem. – Eur. J.*, 2013, **19**, 839.
25 M. Schlangen, J. Neugebauer, M. Reiher, D. Schröder, J. Pitarch Lopez, M. Haryono, F. W. Heinemann, A. Grohmann and H. Schwarz, *J. Am. Chem. Soc.*, 2008, **130**, 4285.
26 J. P. Boyd, E. Irran and A. Grohmann, *Dalton Trans.*, 2012, **41**, 2477.
27 A. Jozwiuk, E. A. Ünal, S. Leopold, J. P. Boyd, M. Haryono, N. Kurowski, F. V. Escobar, P. Hildebrandt, J. Lach, F. W. Heinemann, D. Wiedemann, E. Irran and A. Grohmann, *Eur. J. Inorg. Chem.*, 2012, 3000.
28 M. Schmidt, D. Wiedemann and A. Grohmann, *Inorg. Chim. Acta*, 2011, **374**, 514.
29 M. Schmidt, D. Wiedemann, B. Moubaraki, N. F. Chilton, K. S. Murray, K. R. Vignesh, G. Rajaraman and A. Grohmann, *Eur. J. Inorg. Chem.*, 2013, 958.
30 N. Ortega-Villar, V. M. Ugalde-Saldívar, M. C. Muñoz, L. A. Ortiz-Frade, J. G. Alvarado-Rodríguez, J. A. Real and R. Moreno-Esparza, *Inorg. Chem.*, 2007, **46**, 7285.

31 J. Kaizer, E. J. Klinker, N. Young Oh, J. U. Rohde, W. J. Song, A. Stubna, J. Kim, E. Münck, W. Nam and L. Que Jr., *J. Am. Chem. Soc.*, 2004, **126**, 472.

32 S. Friedrich, M. Schubart, L. H. Gade, I. Scowen, J. Andrew and M. McPartlin, *Chem. Ber./Recl.*, 1997, **130**, 1751.

33 P. Guionneau, C. Brigouleix, Y. Barrans, A. E. Goeta, J.-F. Létard, J. A. K. Howard, J. Gaultier and D. Chasseau, *C. R. Acad. Sci., Ser. IIc: Chim.*, 2001, **4**, 161.

34 M. Haryono, F. W. Heinemann, K. Petukhov, K. Gieb, P. Müller and A. Grohmann, *Eur. J. Inorg. Chem.*, 2009, 2136.

35 P. Guionneau, M. Marchivie, G. Bravic, J.-F. Letard and D. Chasseau, *Top. Curr. Chem.*, 2004, **234**, 97.

36 The 'continuous shape measures *S*' quantify the minimal distance movement that the points of an object have to undergo in order to be transformed into the desired shape; see: H. Zabrodsky, S. Peleg and D. Avnir, *J. Am. Chem. Soc.*, 1992, **114**, 7843.

37 Calculations were performed by using the online service of the Hebrew University of Jerusalem, see: A. Zayit, M. Pinsky, H. Elgavi, C. Dryzun and D. Avnir, *Chirality*, 2011, **23**, 17.

38 D. Casanova, J. Cirera, M. Llunell, P. Alemany, D. Avnir and S. Alvarez, *J. Am. Chem. Soc.*, 2004, **126**, 1755.

39 L. Benhamou, A. Thibon, L. Brelot, M. Lachkar and D. Mandon, *Dalton Trans.*, 2012, **41**, 14369.

40 J. England, G. J. P. Britovsek, N. Rabadia and A. J. P. White, *Inorg. Chem.*, 2007, **46**, 3752.

41 W. J. Geary, *Coord. Chem. Rev.*, 1971, **7**, 81.

42 M. Reiher, O. Salomon and B. A. Hess, *Theor. Chem. Acc.*, 2001, **107**, 48.

43 B. I. Bleaney and B. Bleaney, *Electricity and Magnetism*, Oxford Classical Texts in the Physical Sciences, Oxford University Press, 3rd edn, 2013, vol. 2, p. 456.

44 *Mössbauer spectroscopy*, ed. D. P. E. Dickson and F. J. Berry, Cambridge University Press, 1986.

45 P. Gütlich, E. Bill and A. X. Trautwein, *Mössbauer spectroscopy and transition metal chemistry*, Springer, 2011.

46 S. Hong, Y.-M. Lee, K.-B. Cho, K. Sundaravel, J. Cho, M. J. Kim, W. Shin and W. Nam, *J. Am. Chem. Soc.*, 2011, **133**, 11876.

47 W. L. F. Armarego and C. L. L. Chai, *Purification of Laboratory Chemicals*, Butterworth-Heinemann, Oxford, 6th edn, 2009.

48 Agilent Technologies, *CrysAlisPro Software System: Intelligent Data Collection and Processing Software for Small Molecule and Protein Crystallography*, Agilent Technologies Ltd, Oxford, United Kingdom, 2013.

49 L. Palatinus and G. Chapuis, *J. Appl. Crystallogr.*, 2007, **40**, 786.

50 G. M. Sheldrick, *Acta Crystallogr., Sect. A: Found. Crystallogr.*, 2008, **64**, 112.

51 C. F. Macrae, I. J. Bruno, J. A. Chisholm, P. R. Edgington, P. McCabe, E. Pidcock, L. Rodriguez-Monge, R. Taylor, J. van de Streek and P. A. Wood, *J. Appl. Crystallogr.*, 2008, **41**, 466.

52 P. van der Sluis and A. L. Spek, *Acta Crystallogr., Sect. A: Found. Crystallogr.*, 1990, **46**, 194.

53 H. D. Flack, *Acta Crystallogr., Sect. A: Found. Crystallogr.*, 1983, **39**, 876.

54 R. Ahlrichs, M. Baer, M. Häser, H. Horn and C. Koelmel, *Chem. Phys. Lett.*, 1989, **162**, 165.

55 O. Treutler and R. Ahlrichs, *J. Chem. Phys.*, 1995, **102**, 346.

56 TURBOMOLE V6.3 a development of University of Karlsruhe and Forschungszentrum Karlsruhe GmbH, 1989–2007, TURBOMOLE GmbH, since 2007; available from http://www.turbomole.com.

57 F. Furche and D. Rappoport, *Density functional theory for excited states: equilibrium structure and electronic spectra. Ch. III of "Computational Photochemistry"*, ed. M. Olivucci, vol. 16 of "Computational and Theoretical Chemistry", Elsevier, Amsterdam, 2005.

58 R. Bauernschmitt and R. Ahlrichs, *Chem. Phys. Lett.*, 1996, **256**, 454.

59 R. Bauernschmitt, M. Häser, O. Treutler and R. Ahlrichs, *Chem. Phys. Lett.*, 1997, **264**, 573.

60 F. Weigend and R. Ahlrichs, *Phys. Chem. Chem. Phys.*, 2005, **7**, 3297.

61 A. D. Becke, *J. Chem. Phys.*, 1993, **98**, 5648.

62 C. Lee, W. Yang and R. G. Parr, *Phys. Rev. B: Condens. Matter Mater. Phys.*, 1988, **37**, 785.

63 S. Grimme, J. Antony, S. Ehrlich and H. Krieg, *J. Chem. Phys.*, 2010, **132**, 154104.

64 A. Klamt and G. Schüürmann, *J. Chem. Soc., Perkin Trans. 2*, 1993, 799.

65 V. G. Malkin, O. L. Malkina, R. Reviakine, A. V. Arbuznikov, M. Kaupp, B. Schimmelpfennig, I. Malkin and K. Ruud, *MAG-ReSpect, version 2.1*, 2007.

66 F. Neese, *Inorg. Chim. Acta*, 2002, **337**, 181.